NASA-CR-199425

FINAL
IN-18-CR
10 REF
67499
p 50

FINAL REPORT

for
NASA RESEARCH GRANT
NAG-1-1329

Duplication and Analysis of Meteoroid Damage on LDEF and Advanced Spacecraft Materials

1 January 1993 - 31 December 1994

Auburn University

Space Power Institute
231 Leach Center
Auburn University
Alabama 36849-5320

June 16, 1995

David C. Hill
&
M. Frank Rose

Project Investigators

(NASA-CR-199425) DUPLICATION AND ANALYSIS OF METEOROID DAMAGE ON LDEF AND ADVANCED SPACECRAFT MATERIALS Final Report, 1 Jan. 1993 - Dec. 1994 (Auburn Univ.) 50 p

N96-11222

Unclas

G3/18 0067499

1. INTRODUCTION

The analysis of exposed surfaces on LDEF since its retrieval in 1990 has revealed a wide range of meteoroid and debris (M&D) impact features in the sub-micron to millimeter size range, ranging from quasi-infinite target cratering in LDEF metallic structural members (*e.g.* inter-costals, tray clamps, *etc.*) to non-marginal perforations in metallic experimental surfaces (*e.g.* thin foil detectors, *etc.*). Approximately 34,000 impact features are estimated to exist on the exposed surfaces of LDEF. The vast majority of impact craters in metal substrates exhibit circular footprints, with ~50% retaining impactor residues in varying states of shock processing.

Four papers (Berthoud *et al.*, 1993; Hill *et al.*, 1993; MacKay *et al.*, 1993; Paul, 1993) at the last (3rd) LDEF Post-Retrieval Symposium indicated that understanding of crater geometry and impactor residues as functions of impact velocity and angle can aid in the derivation of impactor trajectories and thus the directional distribution of M&D particles.

The fundamental goals of this project were to duplicate and analyze meteoroid impact damage on spacecraft metallic materials with a view to quantifying the residue retention and oblique impact morphology characteristics. Using the hypervelocity impact test facility established at Auburn University a series of impact tests (normal and oblique incidence) were executed producing consistently high (11-12 km/s) peak impact velocities, the results of which were subsequently analyzed using Scanning Electron Microscope (SEM) and Energy Dispersive X-ray Spectroscopy (EDXS) facilities at Auburn University.

2. OBJECTIVES

The objectives of this program of research have been twofold:

- to simulate and characterize meteoroid and debris hypervelocity impacts
- to engineer and upgrade the Auburn University hypervelocity impact facility.

The major issue for the LDEF meteoroid and debris investigators was that the impact angle is unknown and therefore only a coarse estimate of M&D flux directionality was possible. For impact velocities in excess of ~7 km/s (the vast majority) there is very little residual evidence of impact angle effects, i.e. craters become progressively symmetrical

with no elongation along the impact axis as the impact velocity increases. Figures 1 and 2 show impact craters produced by oblique hypervelocity impacts by olivine particles (diameter = 20 - 100 μm) onto copper targets. Most of the hypervelocity impact sites on the LDEF spacecraft occurred on quasi-infinite metallic surfaces and therefore this project has focused on such targets. Copper was selected as the target material to allow the separation of Mg, Fe elemental residue components from the Cu substrate and the identification of Al contamination from the hypervelocity impact facility drive process.

One way to extract some further directional information is to analyze the impactor residues for any asymmetry in distribution. Figures 3 and 4 show the potential residue distributional effects associated with an oblique hypervelocity impact. The hypothesis is proposed that there will be some degree of quantifiable translation of residue material downrange for oblique impacts which should correlate with the impact velocity and impact angle.

3. EXPERIMENTS

3.1. Hypervelocity Impact Phenomena

When a hypervelocity particle impacts a solid surface and intense flash of light is produced. Early researchers concluded that the impact-induced flash intensity increased with impact velocity, experimental data revealing a functional relationship between velocity, mass and flash intensity (Clark *et al.*, 1959; MacCormack, 1963; Gehring & Warnica, 1963).

The flash comprises two sub-components: (i) a short-duration transient spike attributable to a high pressure, high temperature, dense plasma, with resonance (collision) broadening of line structures, at the impact point, and (ii) a slow-rising, long-duration tail, exhibiting no line-broadening, due to the radiation of a neutral gas expanding from the impact zone (Jean & Rollins, 1970). Observation of the impact flash in the experiments presented here allows the detection of particle impact location and the determination of impact velocity.

The phenomenological model of hypervelocity impact was summarized in the mid-1960's (Gehring *et al.*, 1965), based on the shock structures induced in the impactor and target. Essentially, the impact velocity (in combination with the impactor/target materials) determines the shock compression. The material of the impactor and target are compressed along the shock Hugoniot, increasing entropy, but are released

adiabatically, resulting in a residual temperature of between ~10,000 - 50,000 K on final release which is sufficient to totally vaporize and partially ionize the impactor material plus a significant portion of the material excavated from the impact crater. Material that is not ejected from the impact crater will cool on release and will coat the interior of the crater, including the raised outer crater lips.

3.2. Apparatus

3.2.1. Hypervelocity Launcher

For the experiments reported here the hypervelocity impact facility at the Space Power Institute, Auburn University, Alabama was used. It utilizes the thermal expansion of a plasma produced by an electrically-exploded aluminum foil to accelerate micro-particles in the size range 10 μm - 400 μm diameter. The system is described in detail elsewhere along with its typical operational sequence (Rose *et al.*, 1991). A schematic of the system is shown in Figure 5. The plasma exit velocity at the muzzle has been measured at velocities in excess of 40 km/s using high-speed photographic techniques (IMACON 790 image converter camera). The resultant velocity distribution of micro-particles is dependent on the combination of stored energy, particle size and density, and the number of particles under acceleration.

The launcher is housed in a vacuum chamber pumped to a pressure of ~10^{-6} torr. The micro-particles and residual launcher-drive gas pass along a 7 m long flight tube to a large (1.45 m x 2 m) evacuated (~10^{-6} torr) chamber where they are allowed to impact the target specimen or system under test. Electrical isolation is achieved since all gun electrical activity subsides before particle impact occurs in the target chamber.

Furthermore, the hot plasma drive has relaxed and cooled and is captured by a series of baffles placed in the flight line. As a result, cleanliness is exceptional for a launcher system of this type. A final pre-impact baffle with an aperture correctly sized and positioned to control the impact site location may be inserted into the flight line.

3.2.2. Impact Location and Velocity Diagnostics

The primary diagnostic for the hypervelocity impact experiments is a Hadland-Photonics IMACON 790 Image Converter Camera. The IMACON is utilized in streak mode to detect the incident micro-particles velocities and locations by observing the luminous impact-induced plasma plume. The plasma plume is detected by the IMACON, looking

parallel to the target surface, via a slit that limits the field-of-view to no more than 100 μm at the target surface.

Imaging is triggered to commence at the time of launch of the particles and terminates ~0.5 ms after the arrival of the last hypervelocity particles. The arrival of each hypervelocity particle produces a light flash on the photographic image with a horizontal (time-axis) displacement proportional to the impact velocity. Since the flight distance is known to be 7.05±0.05 m the velocity may be calculated from the time-of-flight.

Impact site location is derived from the vertical displacement of the flash on the streaked photographic image of the slit (see Figure 6). Each impact produces two flash images one displaced positively, the other displaced negatively, from the image horizontal center-line. Light emitting diodes (LEDs) are placed at known positions such that their continuous images provide boundaries on the photographic image corresponding to the impact zone limits.

3.3. Experiments

Each experimental target comprised nine (9) polished copper target plates, each measuring 1.5" X 1.5", arrayed in a in a 3X3 configuration. One set of nine plates was exposed to the hypervelocity particle flux in the impact facility target chamber per experimental shot. On completion of the impact experiment the target was removed from the target chamber and the impact sites located optically, catalogued, and correlated with velocity data derived from the impact experiment streak record.

The plates were then removed from the target fixture and inserted into an SEM for further analysis. Although each site was imaged in real-time, it was not necessary to produce a photographic record of each site. For the purposes of this project it was necessary to obtain quantitative EDX data for each site. Early experiments focused on only two locations within the craters, but as the analysis technique became more sophisticated five locations per crater were analyzed. Impact experiments were repeated to cover a variety of impact angles varying from 30° to 75° relative to the target surface normal vector. Figure 7 shows the analysis site locations for the final set of impact craters analyzed in this project.

Olivine particles (75 μm nominal diameter), having the chemical composition $(Mg:Fe)_2SiO_4$ and a Mg:Fe:Si ratio of ~19:1:10, were launched at copper targets.

Olivine, although higher in density than that usually accepted for meteoroids (ρ = 0.5-1.5 g.cm^{-3}), was chosen as the best meteoroid simulant material that can be accelerated in the hypervelocity impact launcher system. Note that the mass density of olivine is 3.21 g.cm^{-3} and that of copper is 8.92 g.cm^{-3}, resulting in a mass density ratio of ~0.36. This figure corresponds to that for low density (ρ ~ 1 g.cm^{-3}) meteoroids impacting aluminum (ρ ~2.7 g.cm^{-3}) targets. It should be remembered that the density ratio scaling between different materials combinations is a first order approximation only. Peak impact pressure, post-shock mass velocity, and shock velocity all play rôles that will lead to deviations from density ratio scaling at second order level.

A thin Mylar® film (thickness 0.5 μm) was placed in front of the target plates, such that it was always normal to the particle flight path. The hypervelocity particles pass through the film before striking the plate, allowing the particle size to be found (Rose *et al.*, 1992). The film also minimizes gun debris contamination of the target surface.

4. TECHNICAL ANALYSIS

4.1. Meteoroid and Debris Environments

The space particulate environment in low Earth orbit (LEO) comprises two components; the interplanetary dust particulate (IDP) component and the space debris particulate (SDP) component. Two standard models of the IDP component exist: the NASA SP-8013 model (Cour-Palais *et al.*, 1969) and the ESA-Grün model (Grün *et al.*, 1985). The accepted model for the SDP component is the NASA TM-100471 model (Kessler *et al.*, 1988).

For the purposes of this project it was critical to know the impact velocity and impact angle of the SDP and IDP components at any specified spacecraft surface. Impact velocity, combined with impactor and target material type (density and porosity) determines the strength of the shock waves propagating both forward into the target and rearward into the impactor. Grün *et al.* (1985) determined that the average velocity for an IDP entering terrestrial space is 20 km/s, resulting in average impact velocities (for normal incidence) on a spacecraft RAM surface of between 27.8 km/s and 27.4 km/s for the altitude range 250 km - 850 km. The corresponding average impact velocity range (for normal incidence on the WAKE surface) is between 12.2 km/s and 12.8 km/s. Recently, McDonnell (1992) determined the mean normally-resolved impact velocity of IDPs incident on the LDEF spacecraft to be 21.5 km/s for the RAM (East) surface and

11.1 km/s for the WAKE (West) surface. A value of 15.7 km/s was calculated for the North-, South-, and Space-facing surfaces.

For the space debris component, Kessler (1984) computed an impact velocity at 500 km (for 30° and 60° inclination orbits) distribution by analyzing the collision cross-sections for all intersecting debris orbits. The worst-case environment is for polar orbits (inc ~ 90°). The average impact velocity of space debris for a spacecraft in a 28.5° inclination orbit is 9.8 km/s, increasing to 12.5 km/s for a polar orbit. At present, there are no data that verify these models in terms of absolute magnitudes, although it is reasonable to assume that the relative magnitudes are valid based on the orbital mechanics of the scenario.

Recently, Kessler (1992) proposed the existence of small-scale (1-100 μm diameter) space debris in highly elliptic orbits (HEOs) to account for the 13% of impact sites on the WAKE surface of LDEF being of terrestrial origin (Bernhard *et al.*, 1993). Such SDPs are attributed to break-ups of upper stages in geo-synchronous transfer orbits (GTOs) (perigee altitude = 250 km, apogee altitude = 35900 km). The debris produced then cascades down through lower orbits under the combined effects of solar radiation (at apogee) and atmospherics drag (at perigee), resulting in SDP impact velocities in excess of those determined for primarily circular orbits.

A detailed computer model of the IDP flux component was implemented to allow the computation of impact velocity and impact angle distributions for both RAM and WAKE surfaces. Both the NASA and ESA IDP models assume isotropic flux distributions with a geocentric velocity distribution based on the Erickson meteor velocity distribution (Erickson, 1968) (see Figure 8). The model was implemented for a gravity-gradient stabilized spacecraft in a 250 km altitude circular orbit. The model is constructed as follows:

(a) Get a random angle (*theta*) in the X-Z plane measured with respect to the +Z direction (parallel to the spacecraft RAM-direction);
- Get a new random number $-1 \le RAN\# \le 1$
- Compute the angle $theta = inv\cos(RAN\#)$

(b) Get a random angle (*phi*) in the X-Y plane measured with respect to the +X direction (perpendicular to the spacecraft RAM-WAKE axis);
- Get a new random number $0 \le RAN\# \le 1$
- Compute the angle $phi = 2\pi \cdot RAN\#$

NOTE: this combination of (*theta*, *phi*) distributions ensures that the IDPs will arrive isotropically, i.e. there is an equal number of IDPs per unit solid angle arriving at the spacecraft from all directions.

(c) Get a random IDP arrival velocity (V_P) by randomly sampling the Erickson IDP velocity distribution;

- Get a new random number $0 \le RAN\# \le 1$
- For $RAN\# \le X_m$ Solve $F_m(V_P) - RAN\# = 0$

NOTE: The IDP velocity distribution is constructed from 4 velocity distribution functions, $f_m(V_P)$ (m = 1..4), which fit the Erickson data in 4 velocity regimes, where;

$$f_1(V_P) = a_0 + a_1 V_P + a_2 V_P^2 + a_3 V_P^3$$
$$f_2(V_P) = b_0 \exp(-b_1 V_P)$$
$$f_3(V_P) = c_0 + c_1 V_P + c_2 V_P^2 + c_3 V_P^3 + c_4 V_P^4$$
$$f_4(V_P) = d_0 \exp(-d_1 V_P)$$

$$F_1(V_P) = a_0 V_P + \frac{a_1 V_P^2}{2} + \frac{a_2 V_P^3}{3} + \frac{a_3 V_P^4}{4}$$
$$F_2(V_P) = (-b_0/b_1)\exp(-b_1 V_P)$$
$$F_3(V_P) = c_0 V_P + \frac{c_1 V_P^2}{2} + \frac{c_2 V_P^3}{3} + \frac{c_3 V_P^4}{4} + \frac{c_4 V_P^5}{5}$$
$$F_4(V_P) = (-d_0/d_1)\exp(-d_1 V_P)$$

The constants a0, a1, a2, a3, b0, b1, c0, c1, c2, c3, c4, d0, d1, v0, v1, v2, v3, v4 necessary to compute the Erickson distribution are shown in Table 1, below. The functions $F_m(V_P)$ (m = 1..4) are the cumulative distribution functions, i.e. the finite integrals of the functions $f_m(V_P)$. The values X_m (m = 1..4) are computed as follows;

$$X_1 = \frac{\int_{V_0}^{V_1} f_1(v)dv}{X_C}$$
$$X_2 = \frac{\int_{V_0}^{V_1} f_1(v)dv + \int_{V_1}^{V_2} f_2(v)dv}{X_C}$$
$$X_3 = \frac{\int_{V_0}^{V_1} f_1(v)dv + \int_{V_1}^{V_2} f_2(v)dv + \int_{V_2}^{V_3} f_3(v)dv}{X_C}$$
$$X_4 = 1$$

	a	b	c	d	v [km/s]
0	-3.472e+00	1.749e+00	6.429e+00	1.2374+01	9.0
1	6.135e-01	1.290e-01	-4.364e-01	1.290d-01	19.5
2	-3.183e-02	-	1.104e-02	-	52.5
3	5.062e-04	-	-1.235e-04	-	64.5
4	-	-	5.144e-07	-	75.0

Table 1. *Constants for Erickson IDP Velocity Distribution Model*

The normalization constant, X_C, is computed as follows:

$$X_C = \int_{V_0}^{V_1} f_1(v)dv + \int_{V_1}^{V_2} f_2(v)dv + \int_{V_2}^{V_3} f_3(v)dv + \int_{V_3}^{V_4} f_4(v)dv$$

(d) Compute the velocity (V_{rel}) relative to the spacecraft; for each arriving IDP:

$$V_{rel} = \sqrt{(V_{SC} + V_P \cos(theta))^2 + V_P^2 \sin^2(theta)}$$

where V_{SC} = the spacecraft orbital velocity.

(e) Compute the impact angle (*gamma*) relative to the spacecraft surface:

$$gamma = inv\cos\left(\frac{V_{SC} + V_P \cos(theta)}{V_{rel}}\right)$$

(f) Determine the relative number of IDPs striking a specific surface:

- Compute relative flux $f = \dfrac{V_{rel}\cos(gamma)}{V_P}$
- Get new random number $0 \le RAN\# \le f_{max}$

where $f_{max} = \dfrac{V_{Pmin} + V_{SC}}{V_{Pmin}}$

- Remove all IDPs for $RAN\# > f$

NOTE that V_{Pmin} is the minimum arrival velocity (V_P) in the distribution selected from the Erickson distribution; in this case V_{Pmin} = 11.35 km/s.

	Erickson	V_{rel}-RAM	V_{rel}-WAKE	gamma-RAM	gamma-WAKE
MIN	11.4	9.19	5.46	1.12	5.88
MAX	74.6	79.0	70.7	87.7	88.9
Points	8192	2512	406	2512	406
Mean	20.2	23.6	18.3	39.6	53.1
Median	17.5	21.7	14.7	38.7	55.7
RMS	22.1	25.0	21.4	43.7	56.4
Std Dev	9.02	8.02	11.0	18.5	19.2
Std Error	0.100	0.160	0.548	0.369	0.955
Skewness	2.5	2.5	1.9	0.26	-0.44
Kurtosis	8.3	9.6	4.2	-0.59	-0.63

Table 2. *Tabulation of statistical data for the isotropic IDP environment at 250 km altitude as described in the text. V_{rel} = impact velocity; gamma = impact angle with respect to the specific surface normal. The relative fluxes for the RAM surface and the WAKE surface are F = 1.00 and F = 0.16, respectively.*

The results are shown in Figures 9-13. The main outputs of this modeling effort are the impact velocity - impact angle distributions for the RAM and WAKE surfaces (Figures 9 & 10), showing the accessible velocity-angle combinations for the two surfaces. Some combinations are not accessible due to the interaction of spacecraft orbital velocity and IDP arrival velocity. Effectively, the RAM surface aperture increases above 2π steradians as a function of spacecraft velocity whilst the WAKE surface aperture decreases. In the case of the WAKE surface it is clear that if the IDP arrival velocity component parallel to the spacecraft velocity vector is less than the spacecraft velocity then the IDP cannot impact the WAKE surface.

The impact velocity distributions are modified relative to the Erickson meteor arrival velocity distribution by the spacecraft velocity. The mean of the velocity distribution is shifted to higher velocities for the RAM-facing surface, and shifted to lower velocities for the WAKE-facing surface (Figure 11). The dynamics of the system also flattens the WAKE distribution relative to the RAM distribution, spreading the impact velocities more widely. This is manifested by a reduction in the Kurtosis relative to the Erickson distribution. The statistics of the impact velocity and impact angle distributions are shown in Table 2. The Erickson meteor distribution is included for comparison.

The Space Power Institute hypervelocity impact facility currently accelerates particles in the diameter range 50 - 400 μm to velocities in the range 5 - 13 km/s. Under

these conditions, the hypervelocity impact experiments reported here are representative of up to ~30% of IDP impacts on WAKE-facing surfaces, but only ~0.1% of RAM-facing surface impacts (see Figure 13). For space debris particles, the average impact velocity in a circular orbit at 30° inclination is 9.8 km/s and therefore the facility can access up to ~50% of the space debris impacts for RAM and WAKE surfaces combined. To sample these modified impact angle distributions impact experiments were conducted for a variety of impact angles varying from 30° to 75° and including a range of impact velocities from 5 - 13 km/s.

4.2. Energy Dispersive X-ray Analysis

To further understand the effects of impact obliquity and to provide support for the analysis of impact craters recovered from space-exposed quasi-infinite target surfaces, it is necessary to consider the abundance and distribution of impactor residues in the resultant craters. A program of impactor residue analysis using EDXS techniques was, therefore, executed. Samples on which hypervelocity craters were produced were placed in an SEM (Cambridge StereoScan 200) and the X-ray spectrum, derived from the excited states of the atoms present in the target/residue materials, was measured using an EG&G Ortec System 5000 X-ray spectrum analyzer. Compositional calculations were done using the SEM community-standard AutoZAP II program.

For all analysis runs the accelerating voltage was set at 20 kV, which allowed the substrate (copper) signal to become significant. Elapsed live time was 100.00 seconds and the beam current varied from 0.3 nA to 4.6 nA. In all cases the specimen tilt angle was 45.0 degrees with respect to the X-axis and 0.0 degrees with respect to the Y-axis. Insertion depth was 60.0 mm with a typical working depth of between 15-19 mm.

Quantitative data, corrected for substrate contamination (Si, Al), from which relative abundances of elements can be computed for each of the craters, are presented in Appendix A. Careful orientation of the crater with respect to the electron gun axis and the X-ray detector minimizes the geometric effects of deep craters. In section 4.2.1 a procedure for characterizing the effects of geometry is outlined to enable relative abundance computations to be made.

4.2.1. Geometrical Effects

The issue of electron beam and emission X-ray photon shadowing due to the geometry of the impact craters is quite significant. Essentially, the electron beam is incident on the

target surface which is inclined at 45° to the electron beam axis. The direction from the analysis site to the X-ray detector is perpendicular to the electron beam axis, and therefore under normal conditions where the target surface is flat the 45° target inclination maximizes the X-ray photon count. A problem arises when the target surface in the vicinity of the analysis site is not flat, i.e. in the case of an impact crater. By observing the X-ray spectra it becomes apparent that the relative Cu Kα and Lα line intensities vary with location dependent on the amount of electron beam and X-ray photon shadowing. Figures 14 through 18 show the X-ray spectra for the impact site E50-7-M2 (an 8 km/s impact at 45° incidence). It is clear from these spectra that the ratio of Lα to Kα line intensity varies significantly. Since the relative elemental abundance computations are dominated by the Kα counts and the Kα lines for Mg, Si, and Al are close in energy to the Cu Lα line it is necessary to re-scale the counts for Mg, Si, and Al to account for the shadowing effects. The rescaling was accomplished by determined the Cu Lα:Kα ratio for each of the analysis locations (1 - 5) within each crater. Figure 19 shows a plot of the average Lα:Kα peak height ratio as a function of location normalized to location (0) where location (0) is the original undamaged surface of the target. Location (1) includes location (1) and (5) data, i.e. on the crater lips. Location (2) includes location (2) and (4) data, i.e. on the crater interior wall.

4.2.2. Substrate Contamination Effects

The copper substrate is not 100% pure copper as it contains Si inclusions and Al contamination due to the polishing process. To correct for substrate contamination by Si and Al, EDXS analysis was conducted at undamaged target surface sites close to crater sites. Therefore, the relative composition of the substrate was determined for target E50 to be:

$$(Mg, Si, Fe, Al, Cu) \quad = \quad (0.00\%, 4.41\%, 0.00\%, 7.36\%, 88.23\%)$$

Corrections were made to separate the Si substrate and residue components to allow the computation of the residue:substrate ratio. An estimate of the Si substrate component was made for each analysis location by assuming that:

$$\frac{Si_{substrate}}{Cu_{atomic\%}} = \frac{4.41}{88.23}$$

Then;

$$Si_{residue} = Si_{atomic\%} - Si_{substrate}$$

where *atomic%* is the computed atomic percentage of the element at the analysis site.

4.2.3. Data

Four preliminary experimental hypervelocity impact shots were executed, from which resulted in excess of 200 impact sites, identified using an optical scanning system. The minimum identifiable site diameter was ~5 μm. The X-Y locations of all the sites were logged for subsequent correlation with streak record data. Shot D76 (normal incidence) was conducted to confirm gun performance and to determine the typical morphological structures that could be expected for olivine-copper impacts.

Thirteen impact sites from the four shots were then selected for detailed analysis. These, listed below in Table 3, are representative of the numerous impact sites observed. Olivine residue was present in all of the selected craters, implying that residue retention can be expected at normal components of impact velocity up to 12 km/s for the materials combination used in this set of experiments, and also for meteoroids striking aluminum targets if density ratio scaling is assumed to hold. Preliminary modeling of the flux dynamics of flat plates exposed to an *isotropic* meteoroid flux distribution (with the Erickson velocity distribution) indicates that at least 12% of meteoroid craters on the RAM (East) surface should retain residue at levels detectable using EDXS, while at least 65% of WAKE (West) surface craters should retain similar residue.

Site #	***Angle [deg]***	***Velocity [km/s]***	***Residue Appearance***
D76-01-16	0	4.8	white, granular, crystalline
D76-03-10	0	3.0	white, granular, crystalline
D76-03-13	0	9.9	transparent, glassy
D76-05-04	0	8.0	white, granular, crystalline
D76-05-05	0	9.6	transparent, glassy
D76-05-26	0	12.0	transparent, glassy
D76-05-32	0	12.0	transparent, glassy
D80-05-123	45	10.5	transparent, glassy
D78-05-23	60	8.5	white, granular, crystalline
D78-03-17	60	10.5	transparent, glassy
D79-01-02	75	5.7	white, granular, crystalline
D79-03-04	75	12.5	white, granular, crystalline

Table 3. *Preliminary sites selected for detailed SEM and EDXS analysis.*

The normal incidence shot (D76) also provided a baseline for analyzing the residue structure within the craters. Two residue types manifested themselves in this set of craters: white, granular, crystalline; and transparent, smooth, glassy (amorphous). These morphologies are impact velocity dependent, the granular structures being evidence of lower shock intensity while the glassy residue results from shock-induced melting and re-solidification processes.

A further experimental shot, E50, was executed and a detailed analysis of eleven (11) impact craters comprising five (5) EDXS analyses per impact crater was conducted. Rescaling of impact residue quantities was carried out in an attempt to account for the geometrical effects of the crater shape on the electron beam and emission X-ray photon count. The impact angle was set at 45° and the impact velocity spread was 3.7 km/s to 12 km/s. The same two residue types manifested themselves as found in the preliminary impact crater set as shown in Table 4.

Site #	***Angle [deg]***	***Velocity [km/s]***	***Residue Appearance***
E50-03-A	45	12.0	transparent, glassy
E50-06-B	45	11.0	transparent, glassy
E50-06-C	45	10.5	transparent, glassy
E50-07-AE	45	4.6	white, granular, crystalline
E50-08-I	45	8.5	transparent, glassy
E50-08-P	45	7.5	white, granular, crystalline
E50-08-N	45	7.9	transparent, glassy
E50-07-M1	45	8.0	transparent, glassy
E50-07-M2	45	8.0	transparent, glassy
E50-07-M3	45	8.0	transparent, glassy
E50-07-AB	45	3.7	white, granular, crystalline

Table 4. *Sites selected for detailed SEM and EDXS analysis at 5 locations within each crater.*

The resultant data are given in Appendix A. In addition to the quantitative measurements taken at the five crater internal locations, a set of measurements were made at points on the undamaged surface of the target plates. These measurements of relative elemental abundances provide a baseline for the target material itself. Contamination of the copper substrate by both silicon and aluminum was detected and was corrected for in the computations of residue elemental abundances and ratio of residue to substrate at each analysis location.

5. DATA ANALYSIS

5.1. Preliminary Impact Experiments

Quantitative data, corrected for substrate contamination, for the preliminary impact experiments are shown in Table 5. Relative abundances of elements were then computed for each of the craters. Careful orientation of the crater with respect to the electron gun axis and the X-ray detector minimizes the geometric effects of deep craters. For normal incidence impacts location (1) is on the crater inner side wall and location (2) is on the crater lip. For oblique impacts (D78 and D80 sites) location (1) is situated on the leading edge inner side wall and location (2) is on the trailing edge inner side wall. For D79 sites, locations (2) and (3) are in downrange damage areas beyond the main crater trailing (downrange) edge.

SITE #	*Mg*	*Si*	*Fe*	*Cu*	*Mg:Si*	*RES%*	*V_n*	*(2):(1)*
D76-05-26(1)	17.6	5.4	1.1	75.9	8.7	21	12.0	n/a
D76-01-17(1)	28.8	11.0	2.0	58.2	3.4	39	2.9	n/a
D76-01-17(2)	18.7	5.4	0.4	75.5	9.2	22	-	-
D78-03-17(1)	23.7	6.9	2.4	67.0	6.1	30	5.3	1.4±0.2
D78-03-17(2)	33.7	10.9	0.9	54.5	4.0	43	-	-
D78-05-23(1)	25.0	7.3	0.9	66.8	5.8	30	4.3	0.9±0.2
D78-05-23(2)	20.1	8.2	1.4	70.3	4.0	27	-	-
D79-03-04(1)	30.1	10.0	1.7	58.2	4.1	39	3.2	n/a
D79-03-04(2)	23.8	8.1	0.9	67.2	4.7	30	-	n/a
D79-03-04(3)	18.5	5.6	0.5	75.4	8.3	21	-	n/a
D79-01-02(1)	39.5	17.1	2.1	41.3	2.6	57	1.5	n/a
D79-01-02(2)	23.2	7.4	0.9	68.5	5.3	28	-	n/a
D79-01-02(3)	20.4	2.9	0.5	76.2	n/a	23	-	n/a
D80-05-123(1)	15.9	3.9	1.3	78.9	41.8	20	7.4	2.1±0.4
D80-05-123(2)	29.1	10.4	0.7	59.8	3.8	41	-	-

Table 5. *Significant elemental composition by atomic percentage, Mg:Si ratio, and the residue percentage of the total sample. Substrate Si contamination counts were corrected for to obtain the Mg:Si ratio using the measured substrate atomic percentages i.e. Si=4.27%, Cu=95.73%.*

Two representative normal incidence impact sites were selected for more extensive morphological analysis. Site D76-01-17 was a 184±3μm diameter crater, with a circular footprint and raised circumferential lips, exhibiting a p/D ratio of 0.42±0.02, computed from a measured depth of 77±3μm. The impact velocity was 2.9±0.05 km/s. Coating the

interior of this crater was a whitish-green (when viewed optically) granular residue. Conversely, the lips of this crater were coated with a smooth, glassy residue, typical of that found in the interiors of the impact craters produced by faster impactors.

At the other end of the velocity spectrum was site D76-05-26, produced by an olivine fragment traveling at 12.0±0.05 km/s. Again, the circular footprint and raised circumferential lips of a hypervelocity impact are evident. The p/D ratio was computed to be 0.47±0.08 from a crater diameter (D) of 38±2μm and a depth of 18±2μm. The interior of this crater was coated with a smooth, glassy residue, transparent when viewed optically.

The normal incidence crater set was characterized by a division into predominantly granular residues and predominantly glassy residues occurring at an impact velocity of between 8.0 km/s and 9.6 km/s, which corresponds to a shock pressure of between 185 GPa and 240 GPa, using a computational scheme similar to that used by Ang (1990). The implications of this, for site D76-01-17, is that the impactor residue in the crater interior, in granular form, has undergone a significantly less intense shock metamorphosis than that deposited on the crater lips.

The first trend to consider is that between the location (1) analyses, excluding D80-05-123 which results in significantly anomalous data. Normal component of impact velocity (V_n) correlates directly with residue Mg:Si ratio (Figure 20), implying shock-induced fractionation, i.e. the higher the velocity the more silicon is removed from the material matrix. This effect is confirmed by the appearance of the residue, *i.e.* the whitish-green granular residues are the least shock-fractionated (low Mg:Si ratio), whereas the smooth, glassy residues are the most shock-fractionated (high Mg:Si ratio).

Also, residue percentage (RES%), determined by computing the ratio of residue (Mg, Si & Fe) counts to total counts (Mg, Si, Fe & Cu) for location (1) data shows correlation with normal component of velocity (V_n), with the highest velocities producing the lowest residue percentage, *i.e.* the residue layer thickness is apparently reduced for higher velocities (see Figure 21). A further consideration of the ratio of location (1) residue percentage to location (2) residue percentage for impact sites D78-03-17 and D80-05-123 indicates that for oblique angles of incidence more residue tends to be found on the trailing interior surface than the leading interior surface for craters with glassy, amorphous residues. The degree of downrange displacement appears to correlate with V_n with higher normal components of impact velocity producing more

displacement. Consideration of the residue ratio (0.9±0.2) for site D78-05-23 shows that for sites with the white, granular, crystalline residue there is no apparent displacement of residue in the downrange direction.

It is clear from these preliminary experiments that impact angle definitely affects the degree of shock-fractionation experienced by the impactor material and also the relative amounts of residue as a function of location. Effectively, two processes are at work: firstly, shock-fractionation; and, secondly, the displacement of the residue in the downrange direction as a function of the normal component of impact velocity.

5.2. Detailed Analysis of Shot E50

To provide further evidence of shock fractionation and residue distribution within impact craters, 11 craters (E50-series) were analyzed in detail. EDX spectra were obtained and the AutoZAP software used to compute the relative abundances of the major elements at each of five analysis locations within each crater.

The Mg, Si, and Al atomic percentages were rescaled using the rescaling equation derived from the data shown in Figure 19 as follows:

$$X'_N = \frac{X_N}{0.993 - 0.267N} \qquad \text{for } X = \text{Mg, Si, Al; } N = 0..3$$

where X'_N is the rescaled atomic percentage.

The Si and Al atomic percentages were then separated out into $Si_{residue}$, $Si_{substrate}$, $Al_{residue}$, and $Al_{contamination}$ components using the procedure outlined in section 4.2.1 above. The output results include:

- the residue:substrate ratio as a function of normal component of impact velocity at the five analysis locations which allows the degree of residue retention within the crater to be determined;
- the Mg:Si residue ratio as a function of normal component of impact velocity which allows the degree of shock fractionation of the residues to be determined
- the ratio of downrange:uprange residues as a function of impact velocity which shows how the residue is distributed within the crater as a function of impact velocity.

Figures 22-26 show plots of residue:substrate ratio as a function of impact velocity normal component for shot E50 craters at analysis locations (1) through (5). All plots show a downward trend in retained residue as impact velocity increases. The downrange residue ratios, exemplified by Figures 22 and 23, show weak dependencies on impact velocity normal component whereas the uprange locations and the crater bottom show much stronger dependencies.

Considering Figures 27-31 there appears to be correlation between shock fractionation and impact velocity normal component, although it exhibits a weak dependency. These data confirm the findings made during the analysis of the preliminary D-series shots. However, the spread in the data indicates that although shock fractionation is occurring to a greater or lesser extent, the quantification of such a process is far from being complete. It is also possible that shock fractionation effects are largely localized due to variations in shock compression release times. Such variations would result from the irregularity of the impactor in terms of shape, i.e. in these experiments and in space hypervelocity impactors are generally irregular in shape and so shock fractionation cannot be used as a tool for aiding in the determination of impact velocity.

Figure 32, showing the plot of ratio of downrange residue percentage to uprange residue percentage as a function of impact velocity, is extremely interesting as it shows that as impact velocity increases the distribution of residues within the crater becomes more uniform. This is manifested by the convergence to an uprange:downrange residue ratio of unity. Such a convergence correlates with the tendency of impact crater geometry to converge to a hemispherically symmetric geometry as impact velocity increases.

6. CONCLUSIONS

The results from this work indicate that residue retention and residue distribution are definite functions of impact velocity and impact angle. It has been shown that residue percentages in the interior of impact craters depend heavily on the normal component of impact velocity. Likewise, there is also a tendency for residues to exhibit shock fractionation, again dependent upon the normal component of impact velocity. This latter phenomenon is not a pronounced as the residue retention process.

The EDX analysis is accurate to ±0.01 percent under the conditions of the experimental analysis procedures used in this work. This implies that residues may still be detectable within impact craters at normal components of impact velocity up to 15 km/s and perhaps even as high as 20 km/s.

One major finding has been the fact that as impact velocity increases the distribution of residues within the crater becomes more uniform as the uprange:downrange residue ratio converges to unity. This correlates with the hypervelocity impact phenomenon whereby craters become more hemispherically symmetrical as the impact velocity increases.

The results obtained to date suggest that a combination of crater morphology and residue analysis can give evidence of impact azimuth even when the crater profile is near hemispherical as in the case of 30° - 45° impacts. The complex mechanics in oblique impacts where the residue is displaced downrange and undergoes variations in shock fractionation as a function of position have begun to be unraveled. In particular, relative amounts and locations of residue do correlate with impact velocity and can provide limits on that velocity. It is concluded that a combination of analysis techniques can yield further information on impact velocity, direction, and angle of incidence. It remains to be seen whether these findings can be used for LDEF crater analysis where the impact velocities are higher (15-25 km/s) and residues can only be detected by other techniques such as SIMS.

7. REFERENCES

Ang, J.A. (1990). "Impact flash jet initiation phenomenology," *Int. J. Impact Engineering*, **10**, 1-4, pp23-33.

Bernhard, R.P. *et al.* (1993) (with See, T.H. & Hörz, F.). "Projectile compositions and modal frequencies on the 'Chemistry of Micrometeoroids' LDEF experiment," *Proc. 2nd LDEF Post-Retrieval Symp.*, **NASA CP-3194**, pp551-474, (San Diego, CA, USA).

Berthoud, L. *et al.* (1993). "Debris and meteoroid proportions deduced from impact crater residue analysis," *3rd LDEF Post-Retrieval Symp. Abstracts,* **NASA CP-10120**, pp58.

Clark, J.S., *et al.* (1959) (with Kodesch, R.R. & Grow, R.S.). "Spectral analysis of the impact of ultra velocity copper spheres into copper targets," **TR-OSR-13**, University of Utah (Salt Lake City, UT).

Cour-Palais, B.G. *et al.* (1969) (with Whipple, F.L., D'Aiutolo, C.T., Dalton, C.C., Dohnanyi, J.S., Dubin, M., Frost, V.C., Kinard, W.H., Loeffler, I.J., Naumann, R.J., Nysmith, C.R. & Savin, R.C.). "NASA space vehicle design criteria (environment), meteoroid environment model (near Earth to lunar surface)," **NASA SP-8013**.

Erickson, J.E. (1968). "Velocity distribution of sporadic photographic meteors," *J. Geophys. Res.*, **73**, pp3721-3726.

Gehring, J.W. & Warnica, R.L. (1963). "An investigation of the phenomena of impact flash and its potential use as a hit detection and target discrimination technique," *Proc. 6th Hypervelocity Impact Symp.*, **II**, 2, pp. 627-681(Cleveland, OH, USA).

Gehring. J.W. *et al.* (1965) (with Meyers, C.L. & Charest, J.A.). "Experimental studies of impact phenomena and correlation with theoretical models," *Proc. 7th Hypervelocity Impact Symp.*, **III**, pp215-259, (Tampa, FL, USA).

Grün, E. *et al.* (1985) (with Zook, H.A., Fechtig, H. & Giese, R.H.,). "Collisional balance of the meteoritic complex," *ICARUS*, **62**, pp. 244-272.

Hill, D.C. *et al.* (1993). "The effect of impact angle on craters formed by hypervelocity particles," *3rd LDEF Post-Retrieval Symp. Abstracts,* **NASA CP-10120**, pp65.

Jean, B. & Rollins, T.L. (1970). "Radiation from hypervelocity impact generated plasma," *AIAA Journal*, **8**, 10, pp. 1742-1748.

Kessler, D.J. (1984). "Orbital debris environment for space station," NASA Lyndon B. Johnson Space Cnter Report, **NASA JSC 20001**.

Kessler, D.J. (1992). "Origin of orbital debris impacts on LDEF's trailing surfaces," *Proc. 2nd LDEF Post-Retrieval Symp.*, **NASA CP-3194**, pp585-594.

Kessler, D.J. *et al.* (1988) (with Reynolds, R.C. & Anz-Meador, P.D.). "Orbital debris environment for spacecraft designed to operate in low Earth orbit," **NASA TM-100471**.

MacCormack, R.W. (1963). "Investigation of impact flash at low ambient pressure," *Proc. 6th Hypervelocity Impact Symp.*, **II**, 2, pp. 613-625, (Cleveland, OH, USA).

Mackay, N.G. *et al.* (1993). "Experimental investigation of the relationship between impact crater morphology and impacting particle velocity and direction," *3rd LDEF Post-Retrieval Symp. Abstracts,* **NASA CP-10120**, pp66.

Marsh, S.P. (1980). "LASL shock Hugoniot data," University of California Press, Berkeley, CA.

McDonnell, J.A.M. (1992). "LDEF's MAP experimental foil perforations yield hypervelocity impact penetration parameters," *2nd LDEF Post-Retrieval Symp. Abstr.*, **NASA CP-10097**, pp38.

Paul, K. (1993). "Determining orbital particle parameters of impacts into germanium using morphology analysis and calibration data from hypervelocity impact experiments in the laboratory," *3rd LDEF Post-Retrieval Symp. Abstracts,* **NASA CP-10120**, pp67.

Rose, M.F. *et al.* (1991) (with Best, S. and Chaloupka, T.). "Hypervelocity impact facility for simulating the effects of space debris over a wide range of conditions," *Proc. 26th Intersoc. Energy Conv. Engineering Conf.*, **1**, pp. 362-367, (Boston, MA).

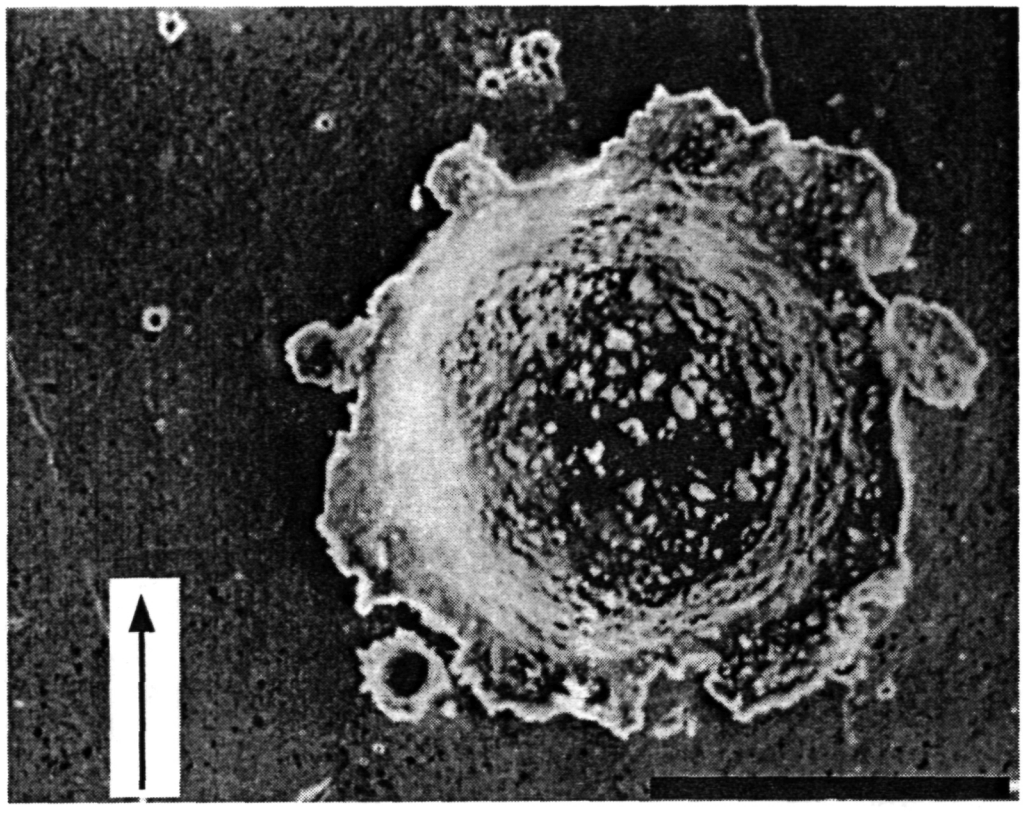

Figure 1. *Photomicrograph of an impact site formed by an olivine particle impacting with a velocity of 7.0 km/s at an angle of 30° with respect to the surface normal. Impact direction is indicated by the arrow. The interior of the crater is coated with olivine residue with visible particle grains. Note the circular footprint and symmetrical lips. [scale bar = 100 μm]*

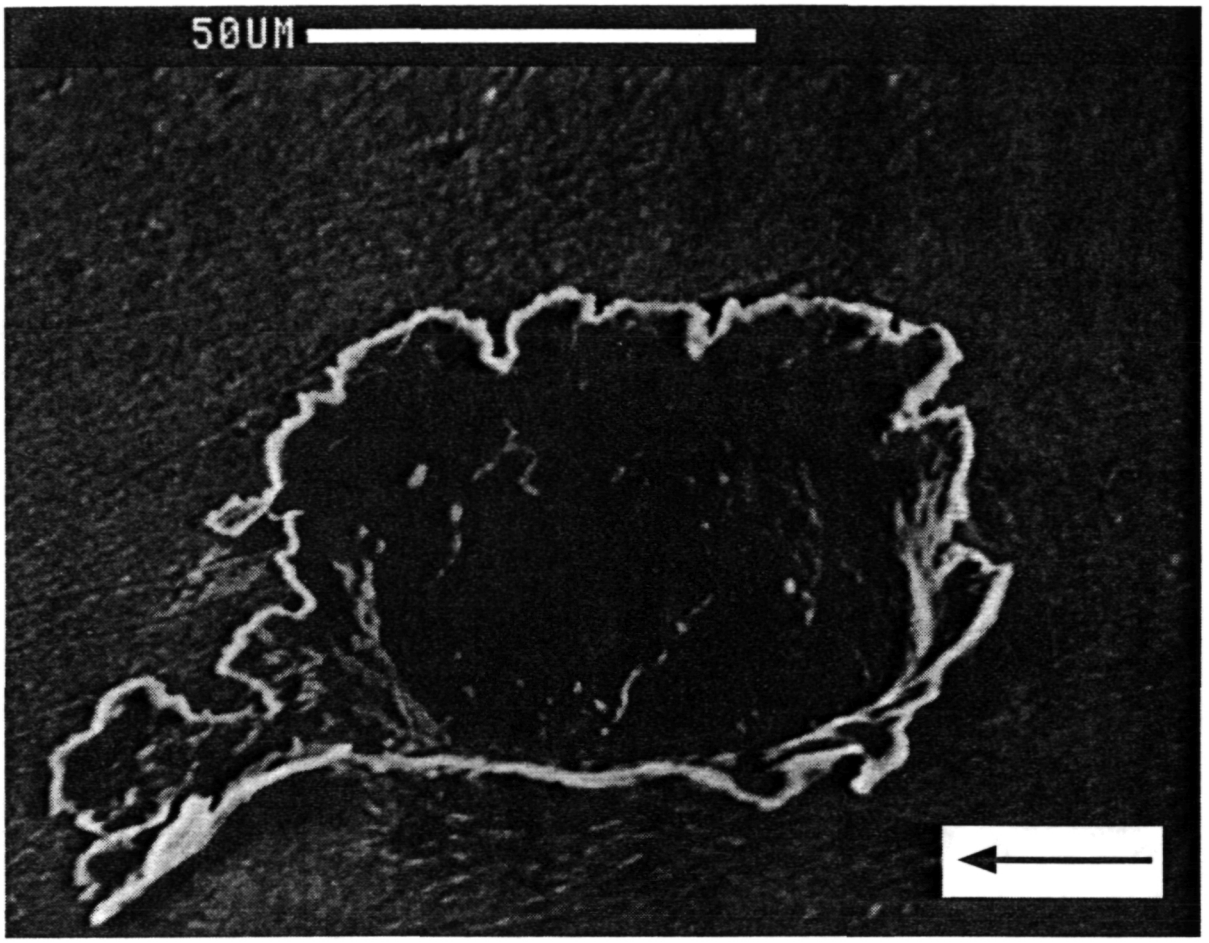

Figure 2. *Photomicrograph of impact site D80-05-123. Impact velocity was 10.5 km/s and angle of incidence was 45°. Impact direction is indicated by the arrow. Note the almost circular footprint and lack of asymmetry between leading edge and trailing edge lips. p/D ratio is 0.48, indicating an almost hemispherical crater which would be insdistinguishable from lower incidence impact craters.*

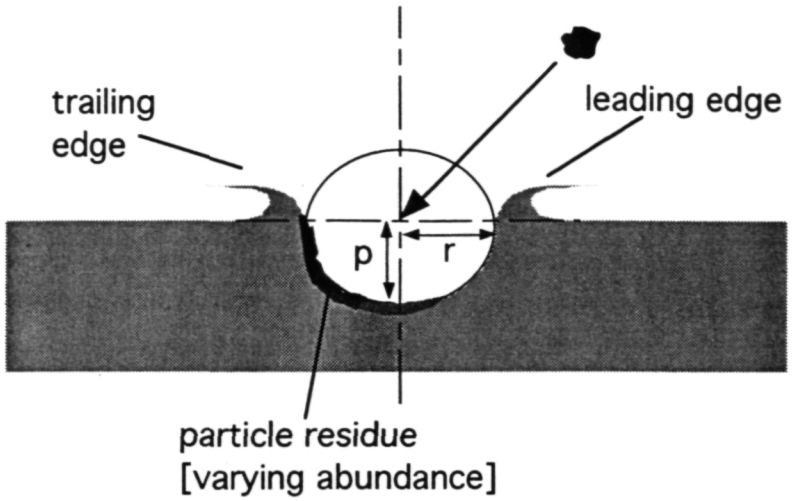

Figure 3. *Schematic of idealized profile of normal-to-45° oblique incidence hypervelocity impact crater. The penetration depth (p) and crater radius (r) are related to the particle diameter (d) and normal component of velocity (v_n) similar to the relationship between penetration depth, particle diameter and impact velocity for normal incidence impacts.*

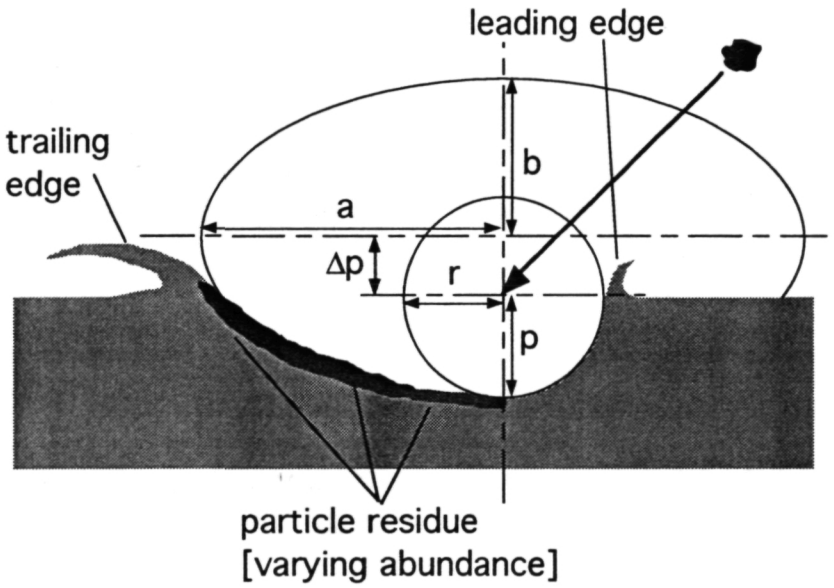

Figure 4. *Schematic of idealized profile of 45°-to-60° oblique hypervelocity impact crater. The minor ellipse (circle, in this case) parameters, penetration depth (p) and crater radius (r) are related to the particle diameter (d) and normal component of velocity (v_n) similar to the relationship between penetration depth, particle diameter, and impact velocity for normal incidence impacts. The major ellipse parameters (a), (b) , and (Δp) are related to the angle of incidence and the shock propagation velocity in the target.*

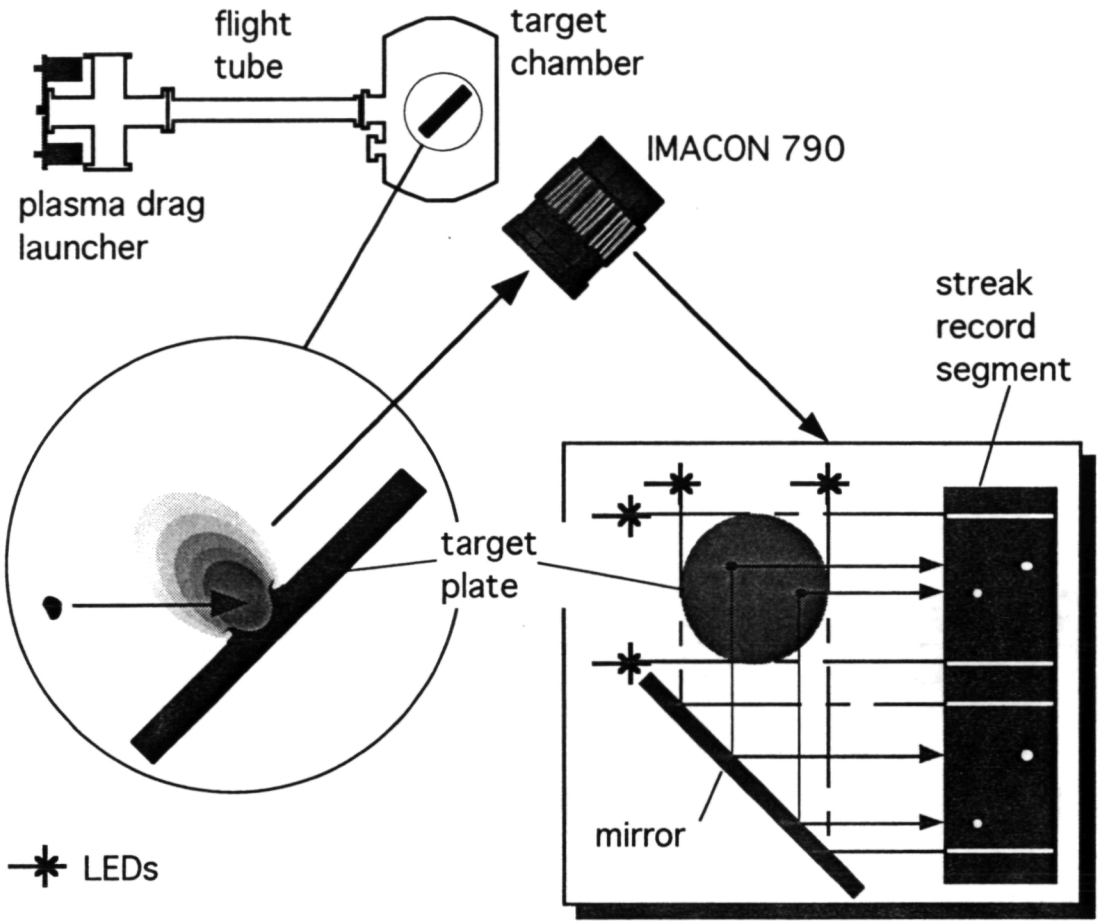

Figure 5. *Schematic of the hypervelocity impact facility and the streak image velocity detection process.*

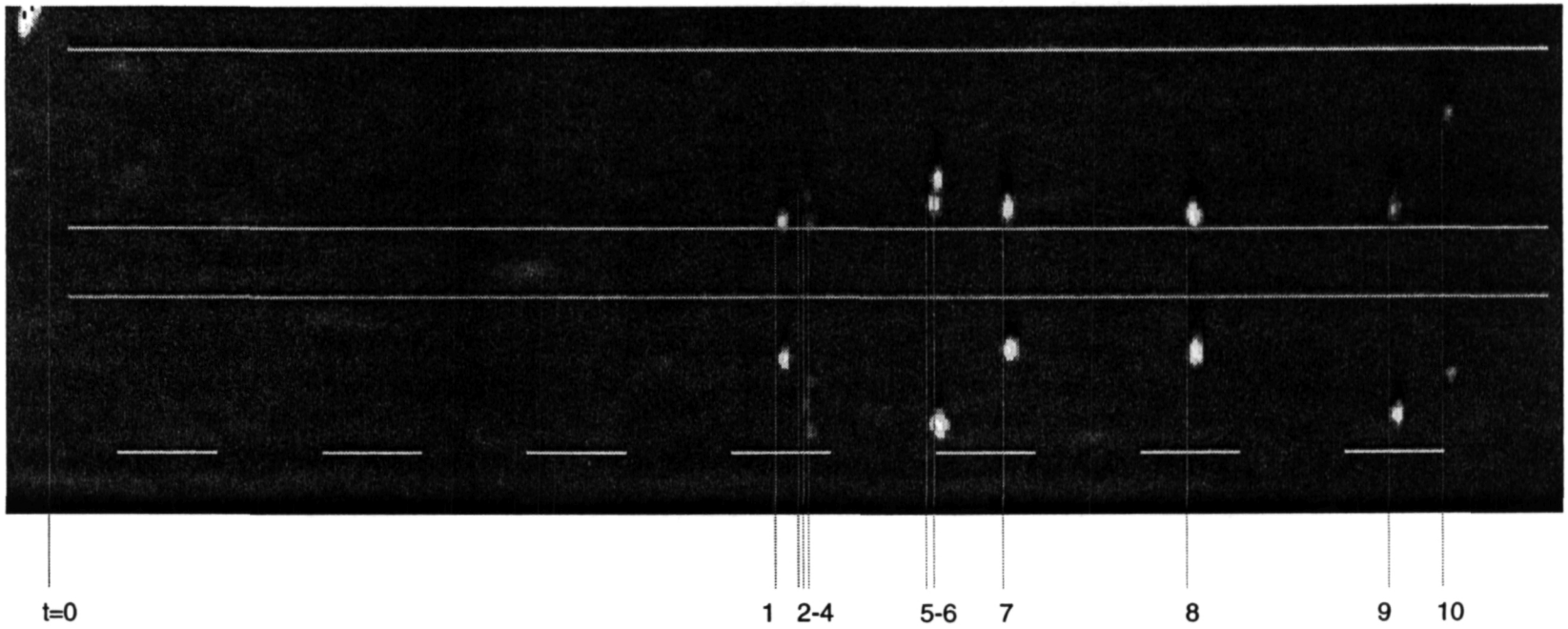

Figure 6. *Gray-scale scanned image of a typical IMACON streak record. TEN impact sites are visible in both the Y-sector (upper half of the image) and the X-sector (lower half of image). Time t=0 is at the left-hand edge with time increasing to the right. The continous horizontal lines are the images of the non-pulsed LEDs, while the intermittent horizontal line is the image of the pulsed LED (T=300μs).*

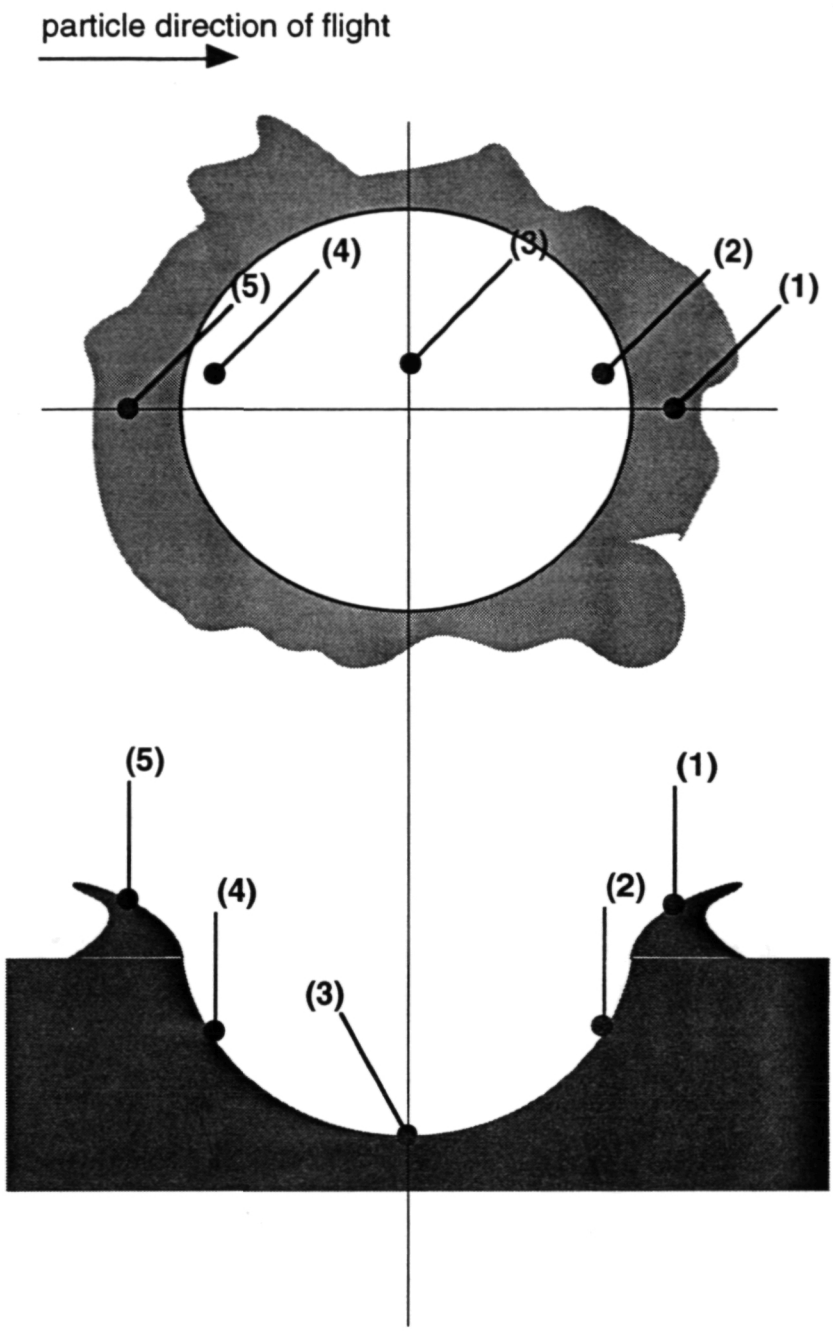

Figure 7. *Typical crater top and side views showing locations of impact site quantitative EDX analyses. Location (1) is on the downrange lip of the crater and location (5) is on the uprange lip.*

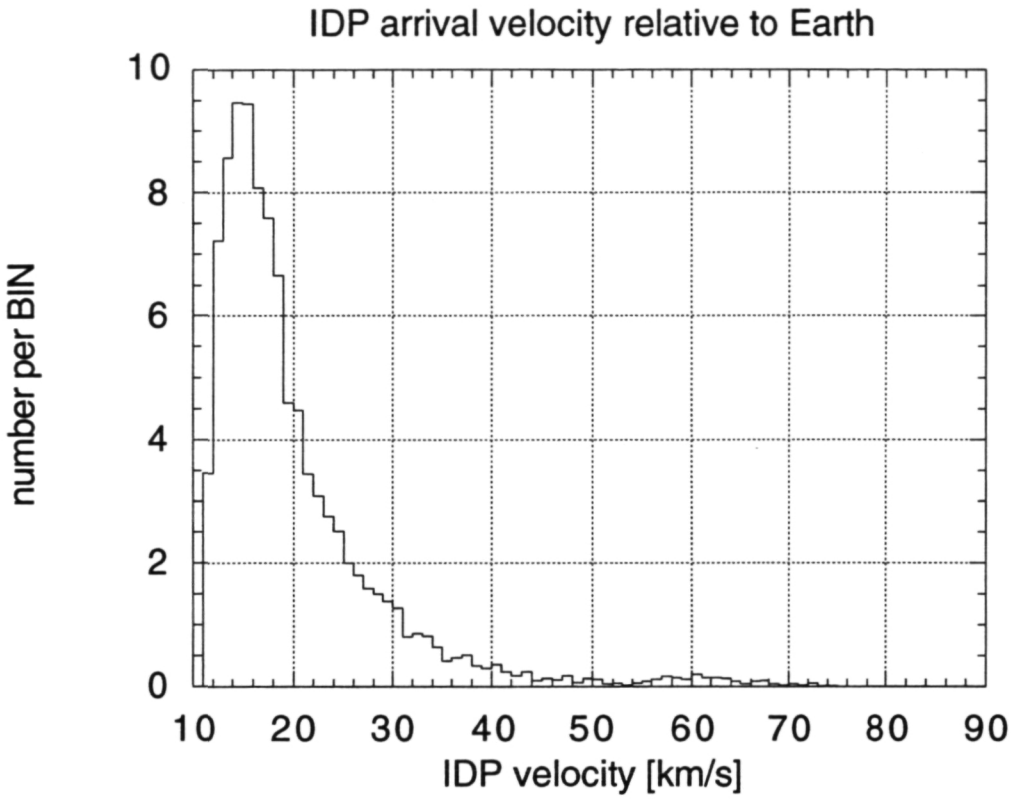

Figure 8. *Binned velocity distribution (Erickson meteor distribution) of IDPs entering near-Earth space.*

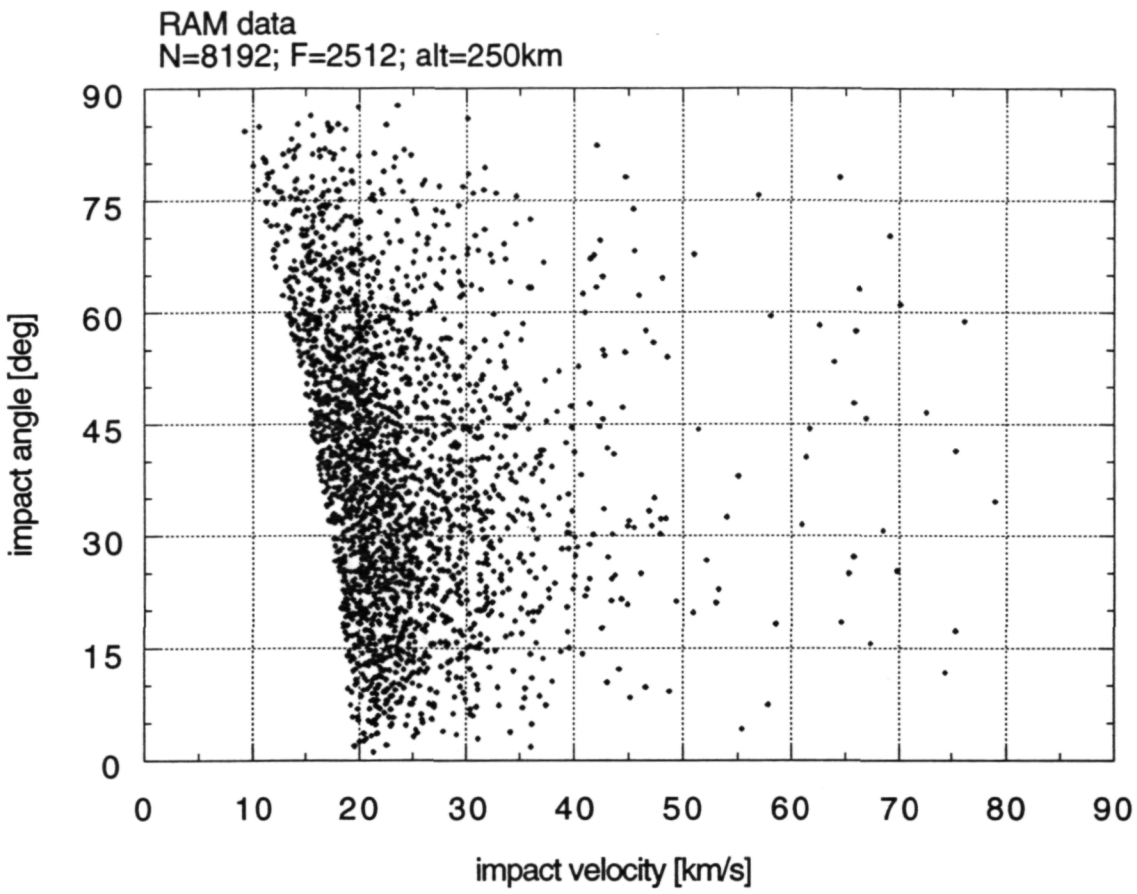

Figure 9. *Plot of impact angle versus impact velocity for a RAM-facing surface of a gravity-gradient stabilized spacecraft in a circular orbit at 250 km altitude. The total flux number, N, is the flux over 4π steradians. The flux, F, is the relative flux for the RAM-facing surface.*

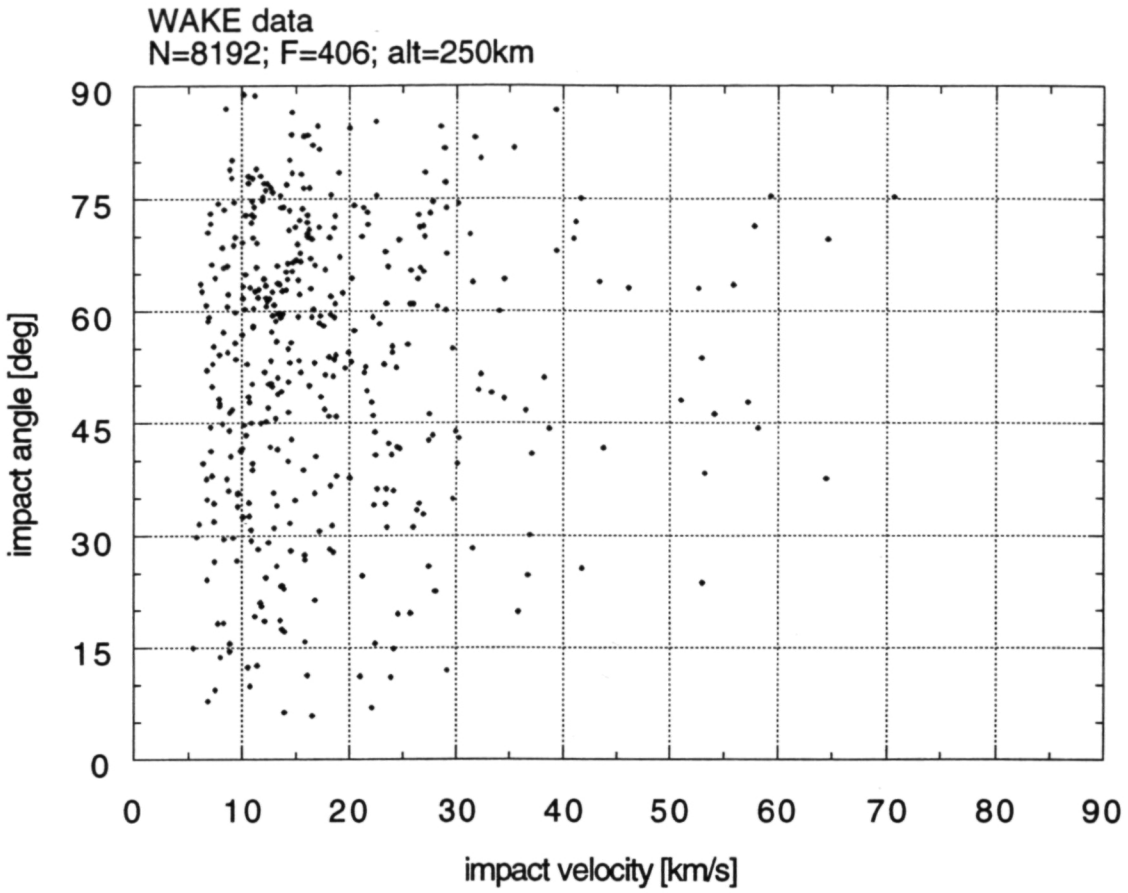

Figure 10. *Plot of impact angle versus impact velocity for a WAKE-facing surface of a gravity-gradient stabilized spacecraft in a circular orbit at 250 km altitude. The total flux number, N, is the flux over 4π steradians. The flux, F, is the relative flux for the WAKE-facing surface.*

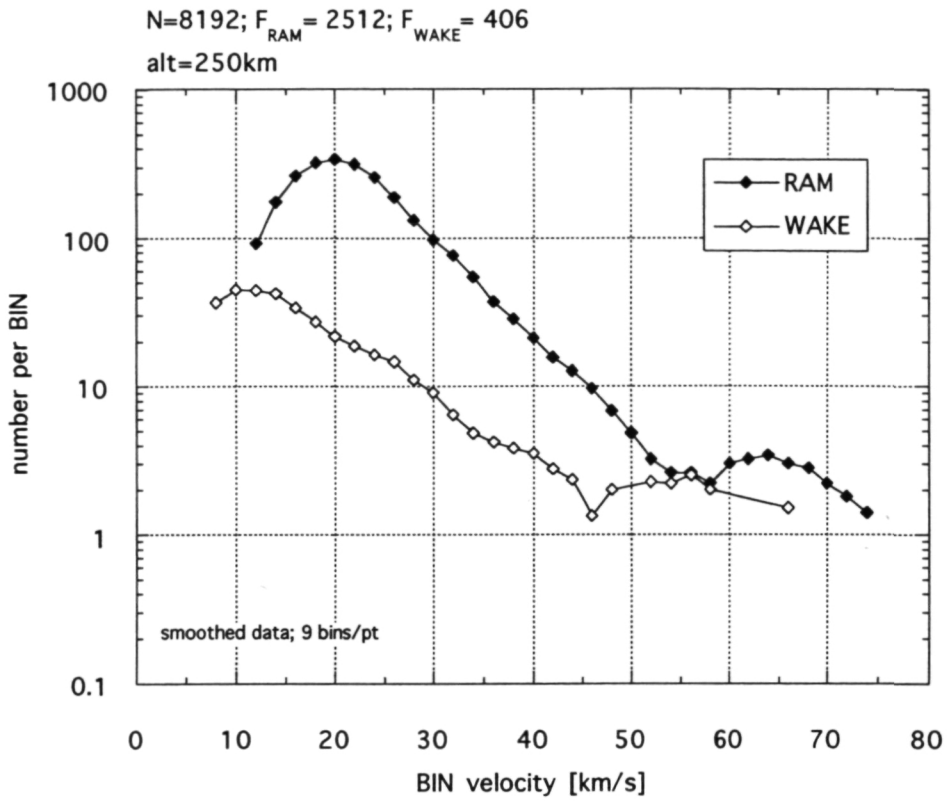

Figure 11. *Velocity distributions for RAM- and WAKE-facing surfaces on a gravity-gradient stabilized spacecraft in a circular orbit at 250 km altitude.*

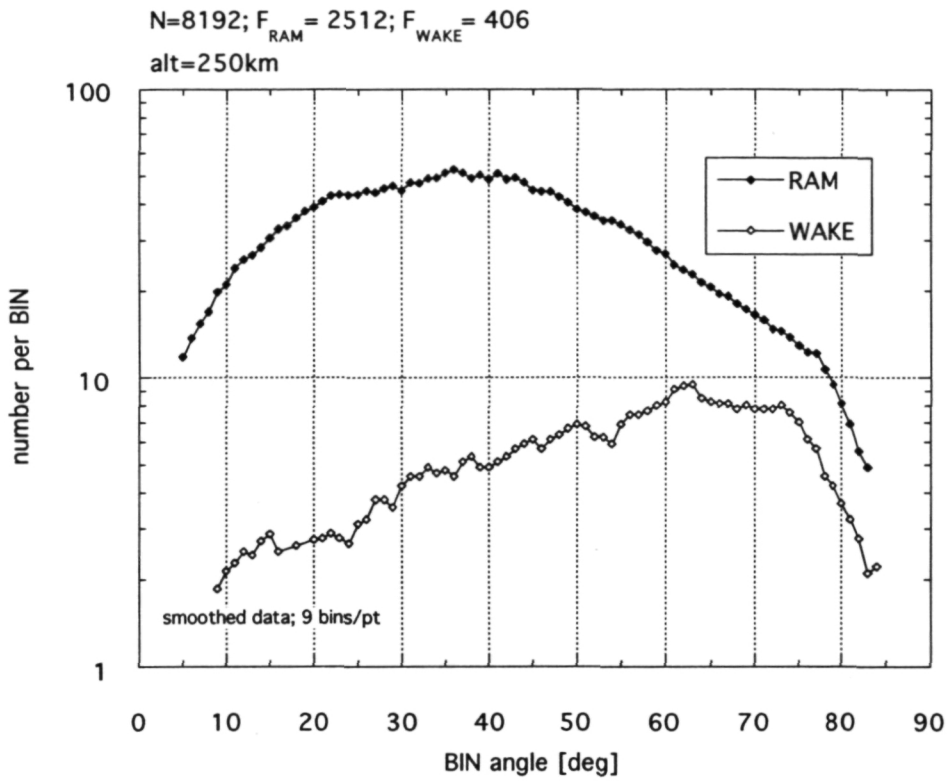

Figure 12. *Impact angle distributions for RAM- and WAKE-facing surfaces on a gravity-gradient stabilized spacecraft in a circular orbit at 250 km altitude.*

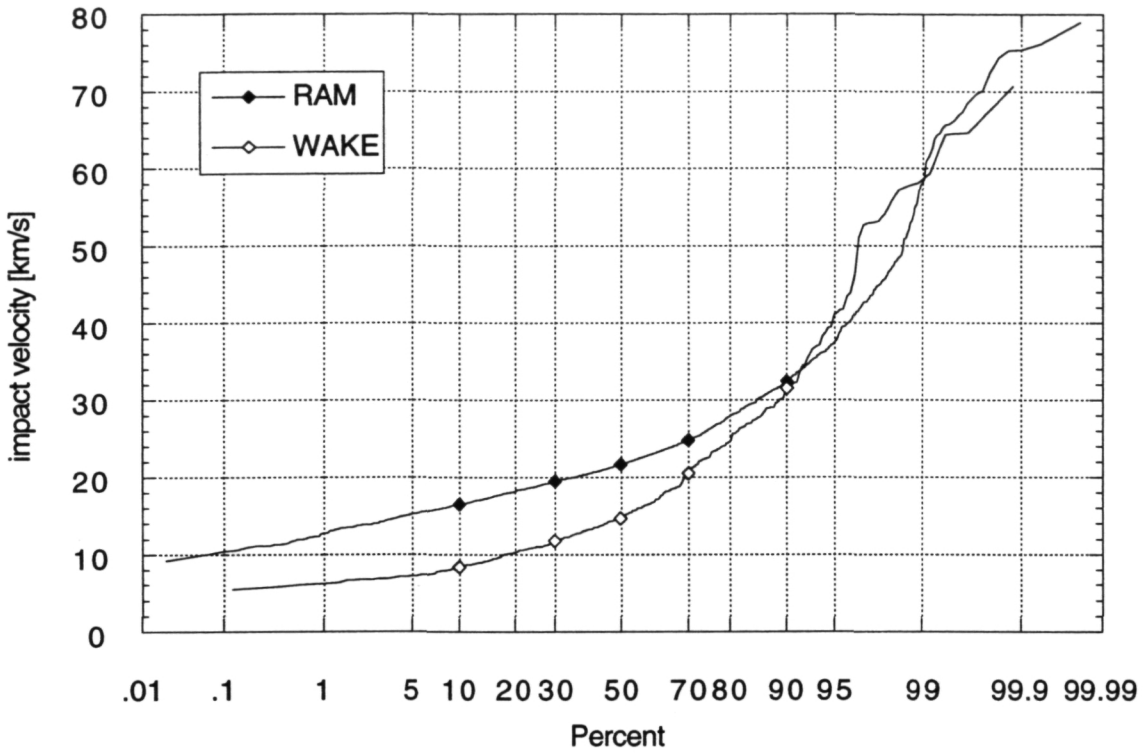

Figure 13. *Probability distribution plot for impact velocity on both RAM and WAKE surfaces for a gravity-gradient stabilized spacecraft in a circular orbit at an altitude of 250 km.*

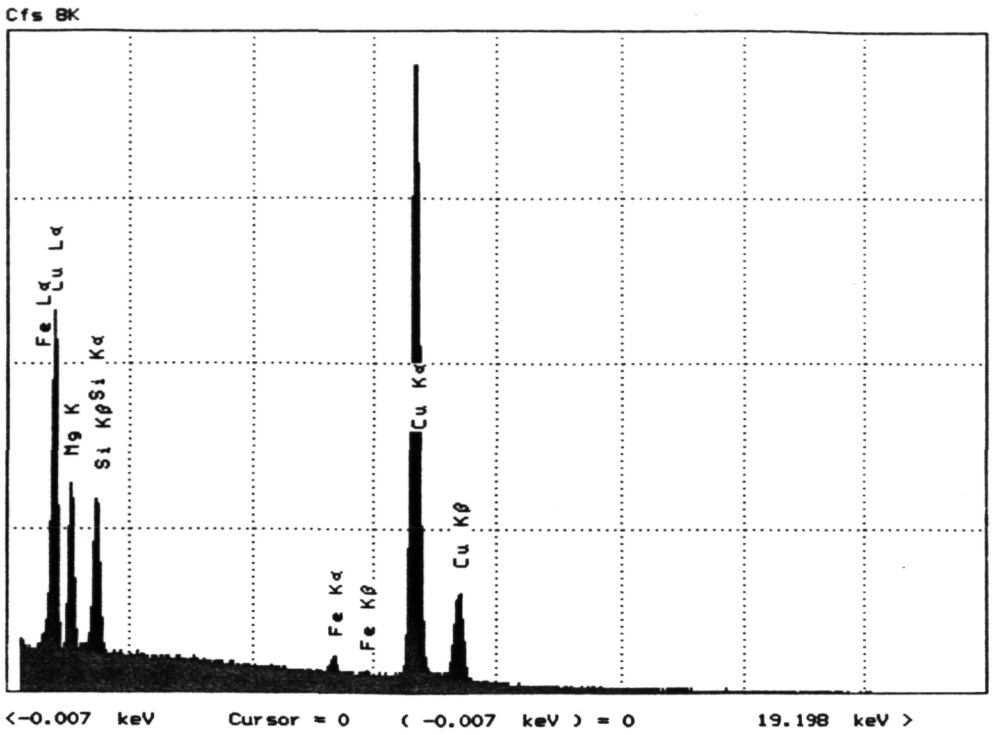

Figure 14. *EDX spectrum for analysis location E50-7-M2-1. The Lα:Kα peak height ratio is 0.611.*

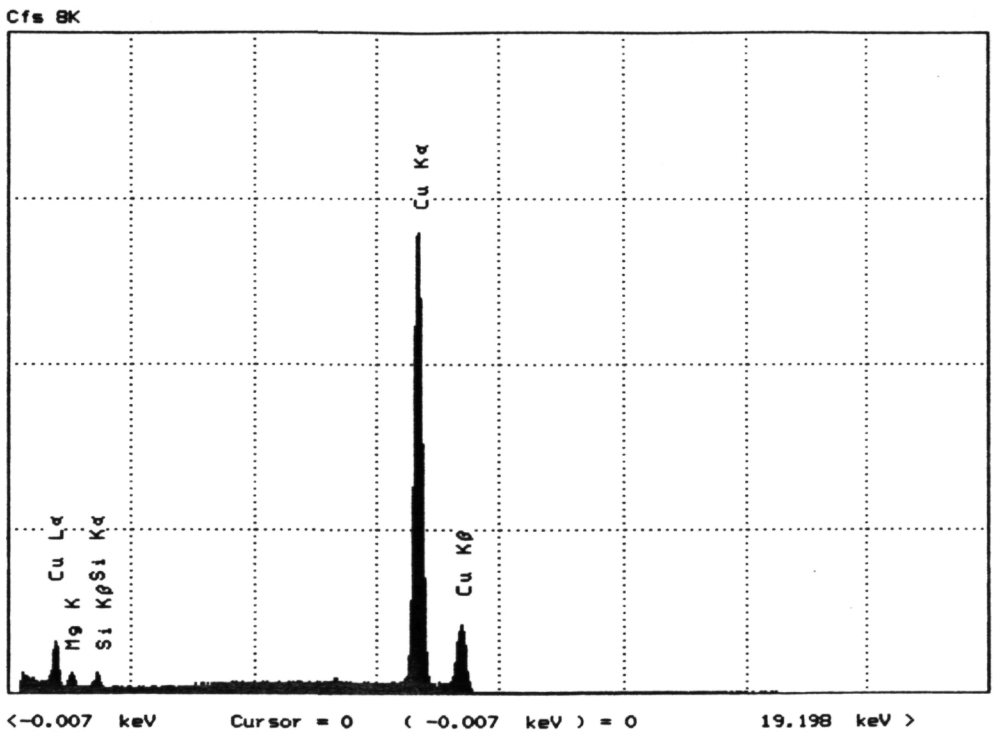

Figure 15. *EDX spectrum for analysis location E50-7-M2-2. The Lα:Kα peak height ratio is 0.112.*

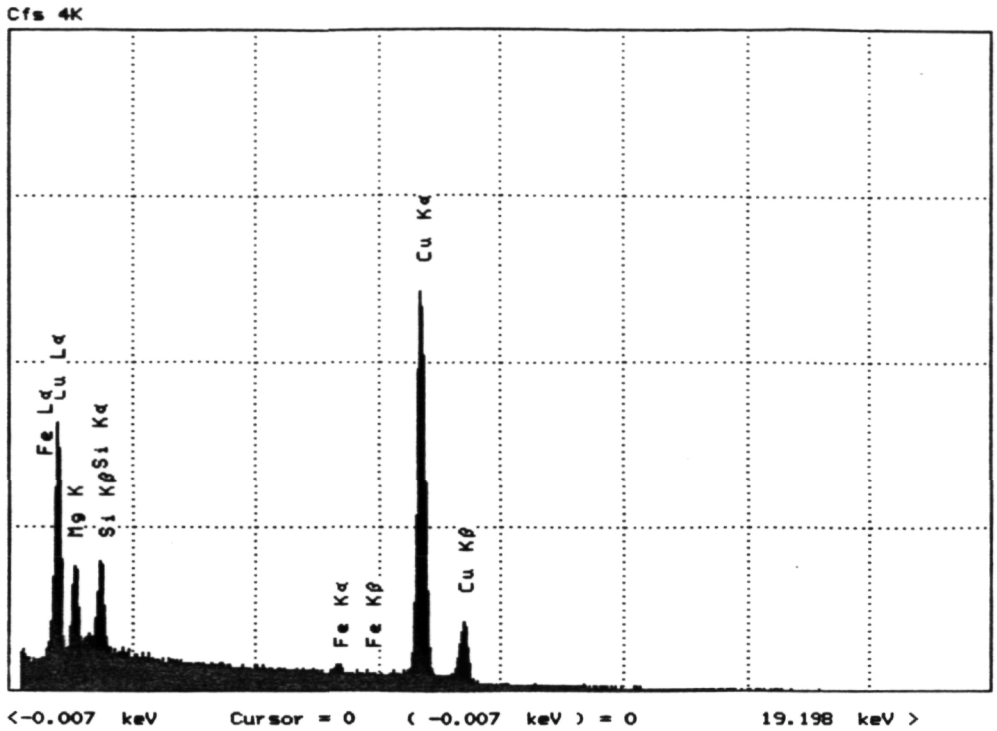

Figure 16. *EDX spectrum for analysis location E50-7-M2-3. The Lα:Kα peak height ratio is 0.671.*

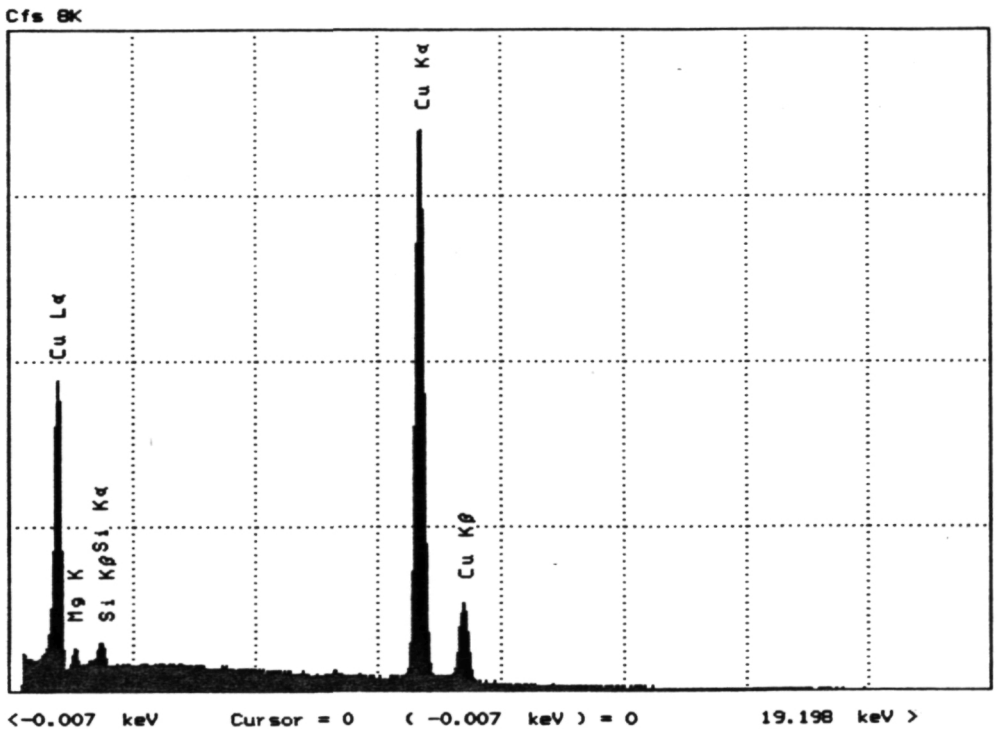

Figure 17. *EDX spectrum for analysis location E50-7-M2-4. The Lα:Kα peak height ratio is 0.557.*

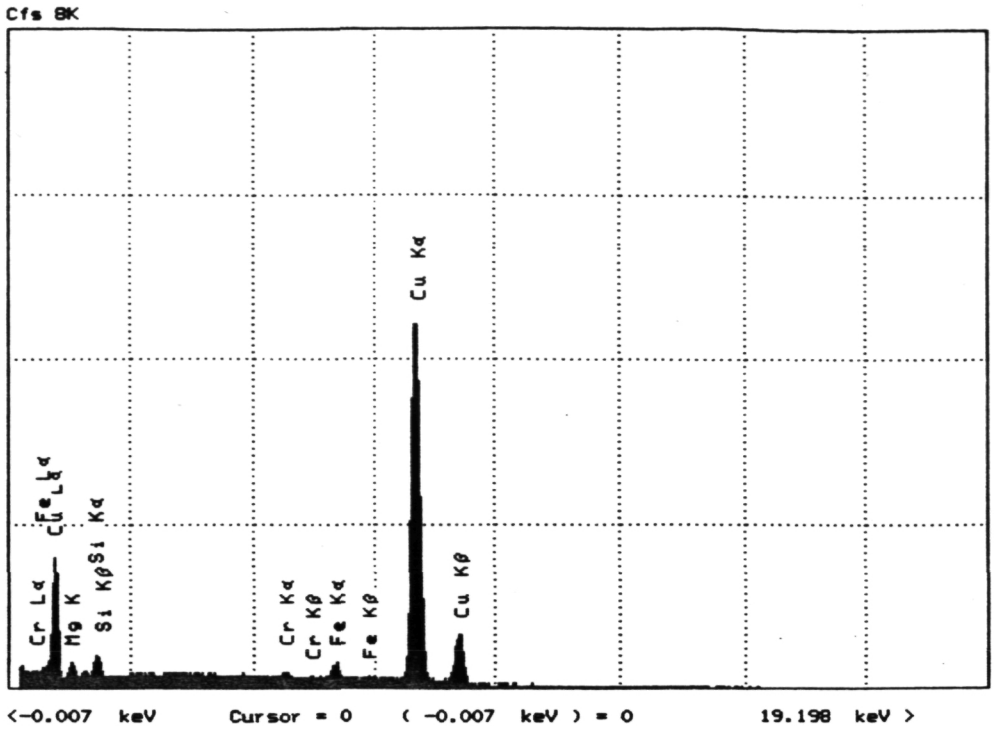

Figure 18. *EDX spectrum for analysis location E50-7-M2-5. The Lα:Kα peak height ratio is 0.362.*

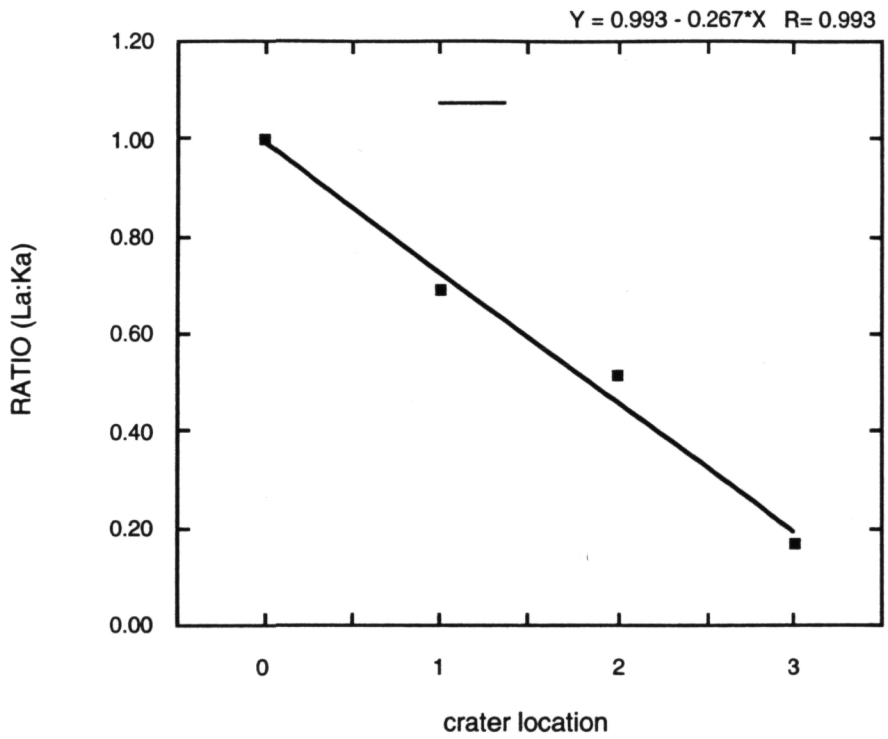

Figure 19. *Normalized average Lα:Kα peak height ratio as a function of EDX analysis location. Location (0) is at the undamaged target surface where the electron beam and X-ray detector field of view is unobstructed by the crater geometry. Location (1) includes location (5) data, i.e. on the crater lip; location (2) includes location (4) data, i.e. on the crater interior wall. Location (3) is at the bottom of the crater*

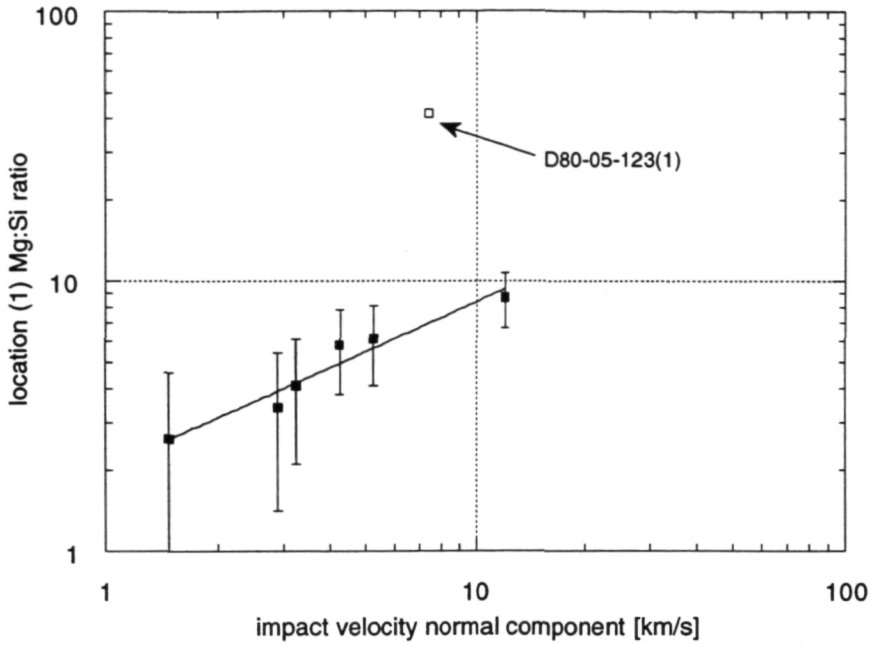

Figure 20. *Graph of location (1) residues Mg:Si ratio showing the increase of shock fractionation with increasing normal component of impact velocity (V_n). This data is for the preliminary D-series shots.*

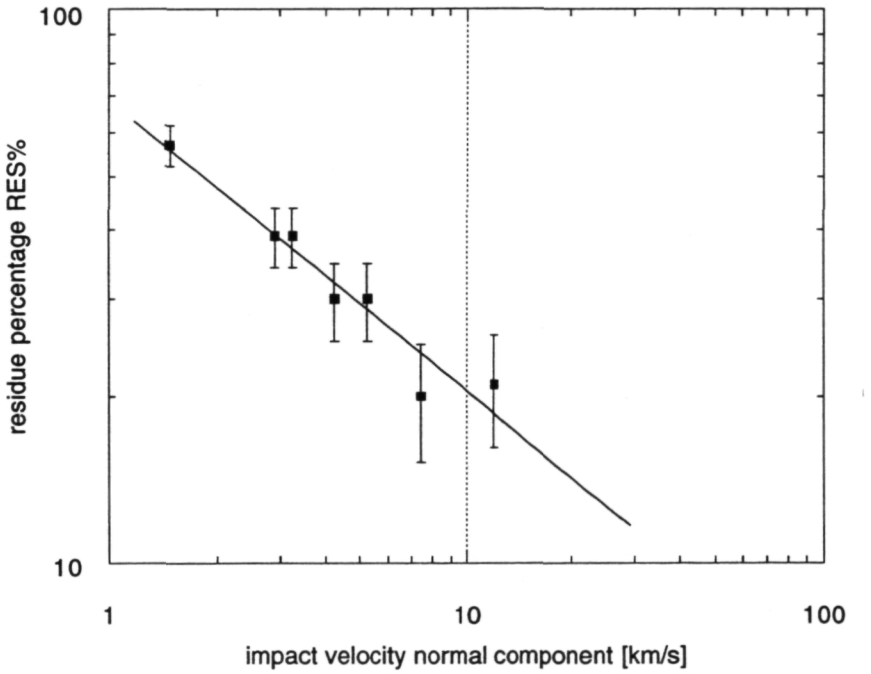

Figure 21. *Graph of location (1) residue percentage versus impact velocity normal component (V_n). This data is for the preliminary D-series shots.*

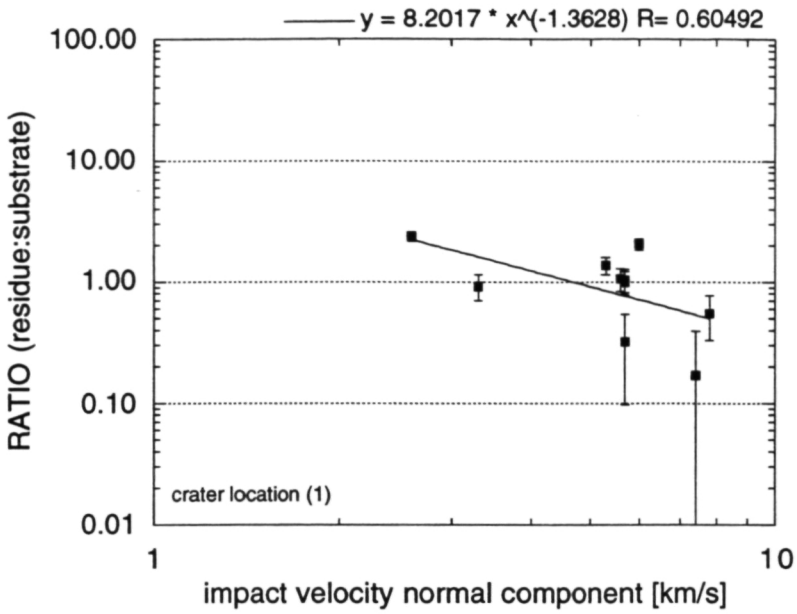

Figure 22. *Plot of residue:substrate ratio as a function of impact velocity normal component for shot E50 craters at analysis location (1), i.e. on the downrange crater lip interior.*

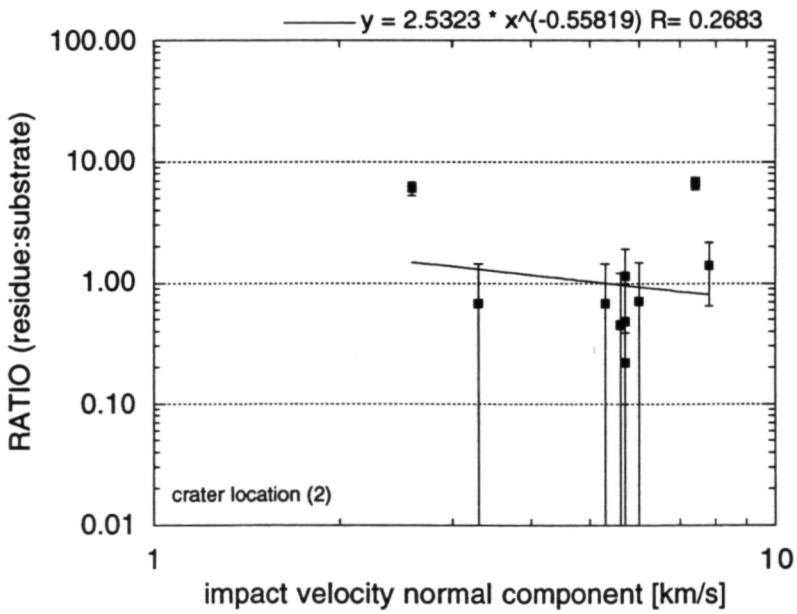

Figure 23. *Plot of residue:substrate ratio as a function of impact velocity normal component for shot E50 craters at analysis location (2), i.e. on the downrange crater interior wall.*

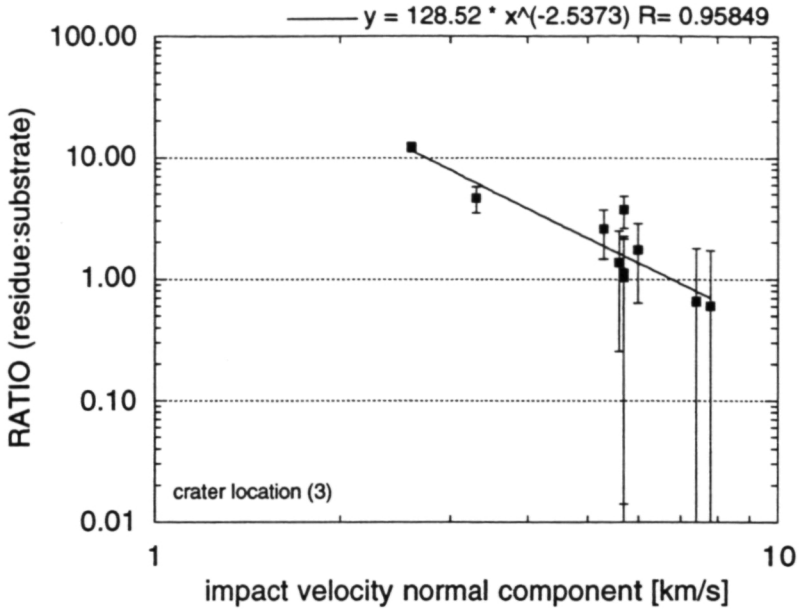

Figure 24. *Plot of residue:substrate ratio as a function of impact velocity normal component for shot E50 craters at analysis location (3), i.e. in the bottom of the crater.*

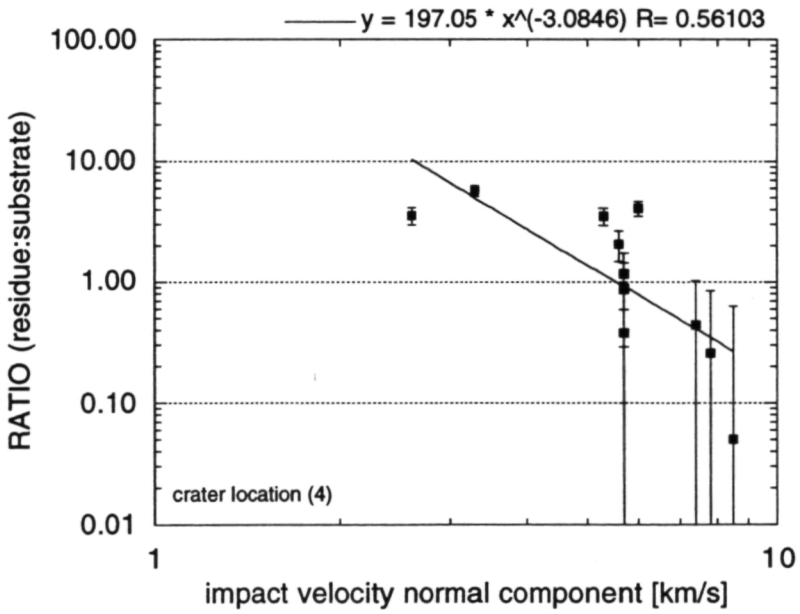

Figure 25. *Plot of residue:substrate ratio as a function of impact velocity normal component for shot E50 craters at analysis location (4), i.e. on the uprange crater interior wall.*

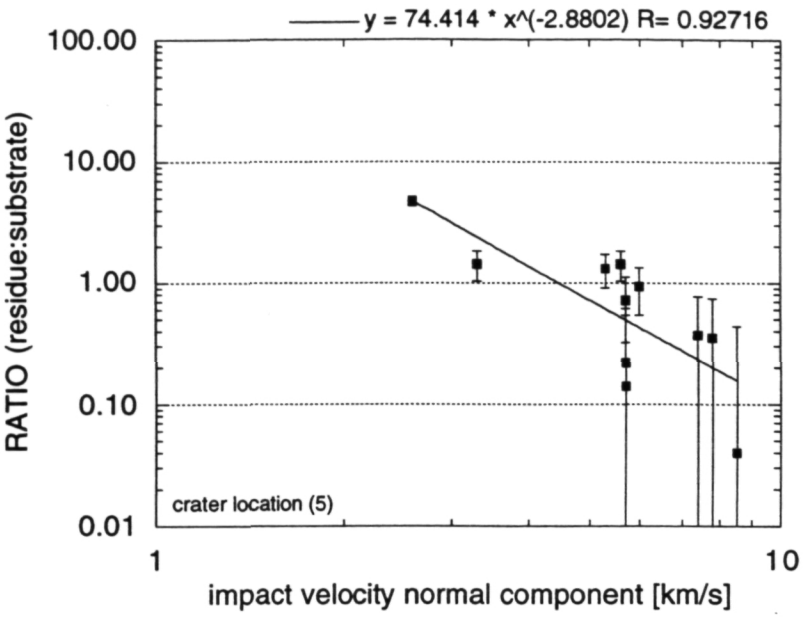

Figure 26. *Plot of residue:substrate ratio as a function of impact velocity normal component for shot E50 craters at analysis location (5), i.e. on the uprange crater lip interior .*

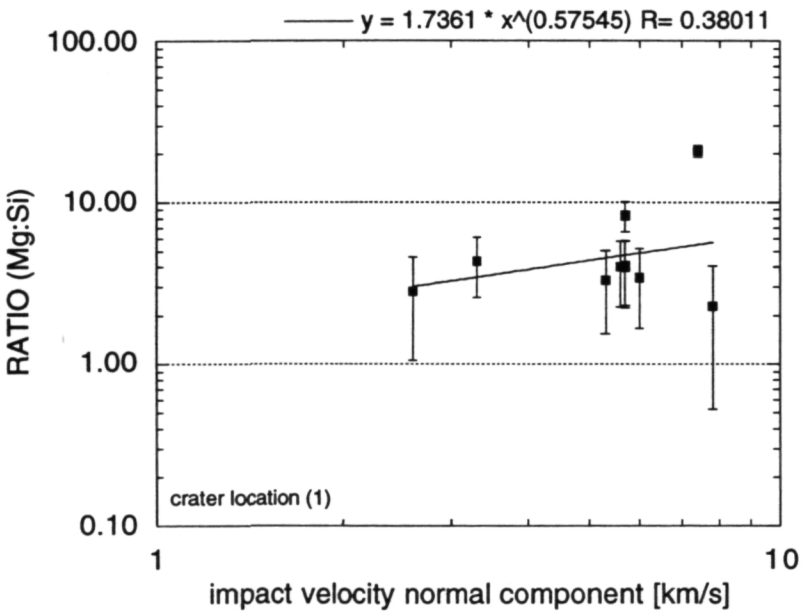

Figure 27. *Plot of residue Mg:Si ratio as a function of impact velocity normal component for shot E50 craters at analysis location (1), i.e. on the downrange crater lip interior .*

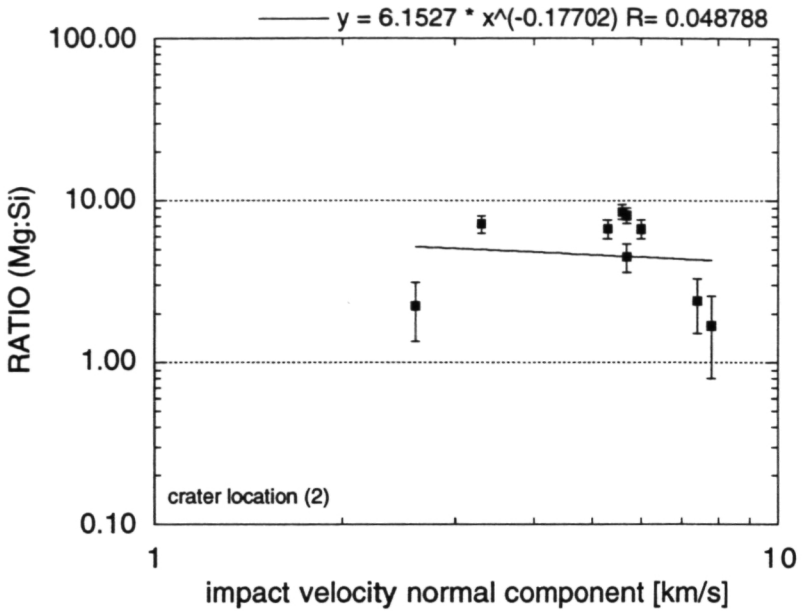

Figure 28. *Plot of residue Mg:Si ratio as a function of impact velocity normal component for shot E50 craters at analysis location (2), i.e. on the downrange crater interior wall.*

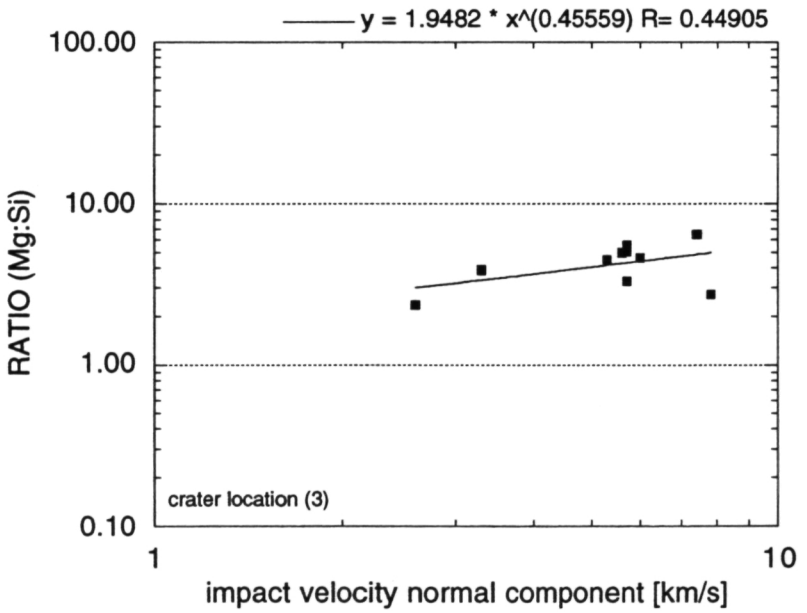

Figure 29. *Plot of residue Mg:Si ratio as a function of impact velocity normal component for shot E50 craters at analysis location (3), i.e. in the bottom of the crater.*

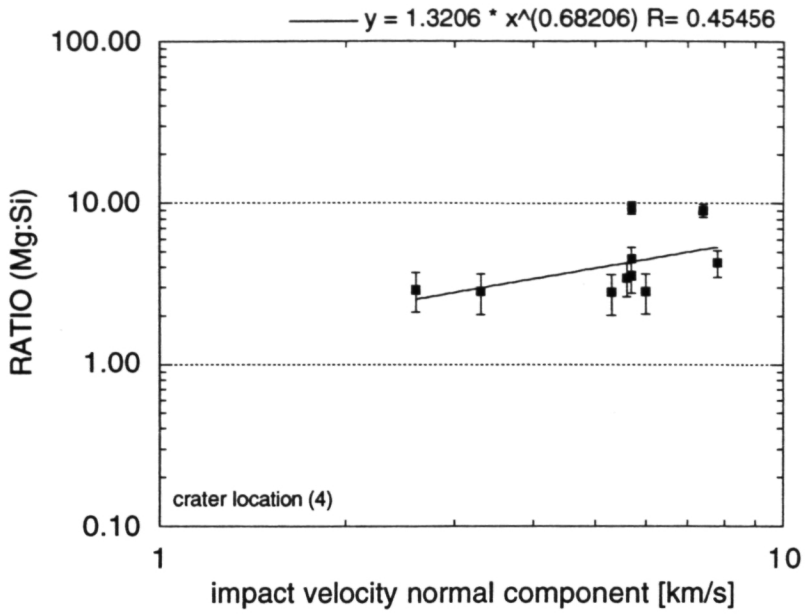

Figure 30. *Plot of residue Mg:Si ratio as a function of impact velocity normal component for shot E50 craters at analysis location (4), i.e. on the uprange crater interior wall.*

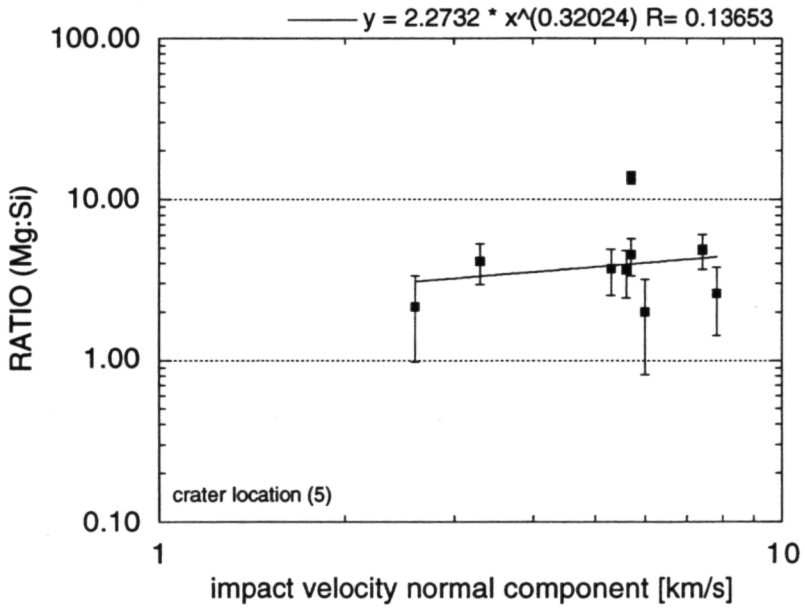

Figure 31. *Plot of residue Mg:Si ratio as a function of impact velocity normal component for shot E50 craters at analysis location (5), i.e. on the uprange crater lip interior .*

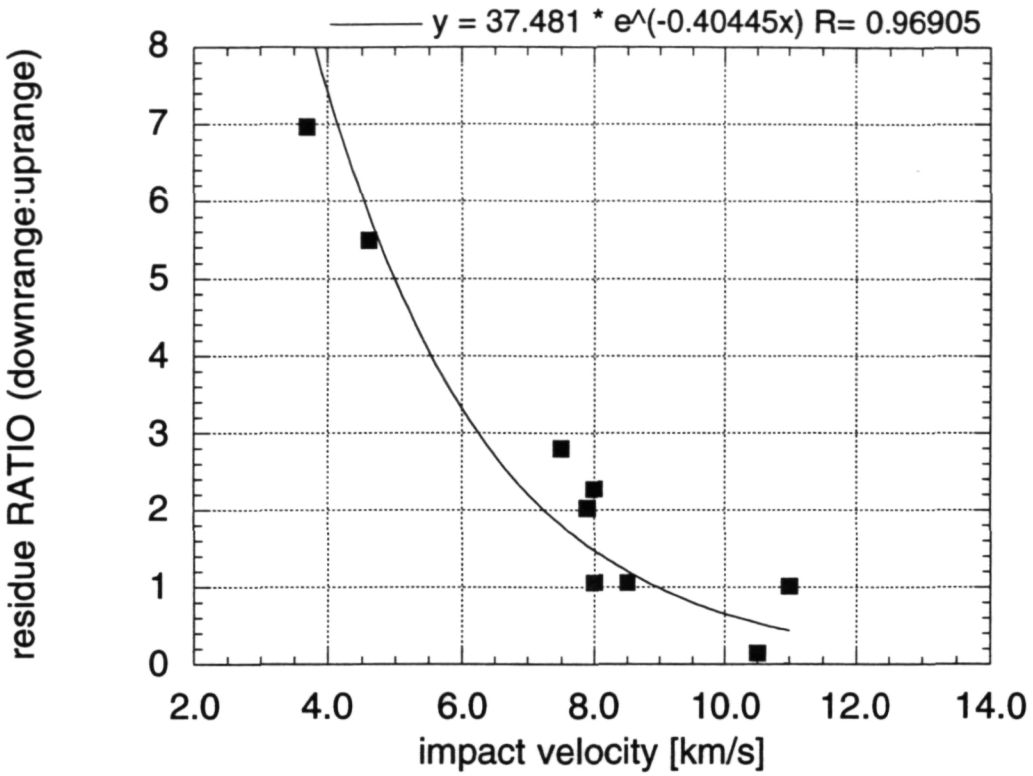

Figure 32. *Plot of ratio of downrange residue percentage to uprange residue percentage as a function of impact velocity.*

APPENDIX A: Shot E50 EDXS Data

SUBSTRATE	Mg	Si	Fe	Al	Cu	other	totals						
sub_1	0.00	3.42	0.00	7.49	89.09	0.00	100.00						
sub_2	0.00	4.44	0.00	8.33	87.23	0.00	100.00						
sub_3	0.00	5.37	0.00	6.27	88.36	0.00	100.00						
sub_avg	0.00	4.41	0.00	7.36	88.23	0.00	100.00						
SITE ID	loc#	SF	V	Mg	Mg_sca	Si	Si_sca	Fe	Al	Al_sca	Cu	other	total
E50-3-A1	1	0.726	12.0	0.00	0.00	2.05	2.82	0.00	4.36	6.01	93.46	0.13	102.42
E50-3-A2	2	0.459	12.0	0.00	0.00	0.00	0.00	0.00	2.57	5.60	98.89	0.00	104.49
E50-3-A3	3	0.192	12.0	0.00	0.00	0.00	0.00	0.00	0.00	0.00	100.00	0.00	100.00
E50-3-A4	4	0.459	12.0	0.00	0.00	4.18	9.11	0.00	9.55	20.81	86.27	0.00	116.18
E50-3-A5	5	0.726	12.0	0.00	0.00	5.68	7.82	0.00	14.50	19.97	79.83	0.00	107.63
SITE ID	Mg	Si	Fe	Al	Cu	Si_sub	Si_res	Al_sub	Al_con		RES:SUB	Mg:Si	
E50-3-A1	0.0	2.8	0.0	5.9	91.3	4.6	-1.8	7.6	-1.8		-0.02	0.00	
E50-3-A2	0.0	0.0	0.0	5.4	94.6	4.7	-4.7	7.9	-2.5		-0.04	0.00	
E50-3-A3	0.0	0.0	0.0	0.0	100.0	5.0	-5.0	0.0	0.0		-0.05	0.00	
E50-3-A4	0.0	7.8	0.0	17.9	74.3	3.7	4.1	6.2	11.7		0.05	0.00	
E50-3-A5	0.0	7.3	0.0	18.6	74.2	3.7	3.6	6.2	12.4		0.04	0.00	
SITE ID	loc#	SF	V	Mg	Mg_sca	Si	Si_sca	Fe	Al	Al_sca	Cu	other	total
E50-6-B1	1	0.726	11.0	19.55	26.93	10.82	14.90	0.00	6.68	9.20	62.30	0.64	113.97
E50-6-B2	2	0.459	11.0	24.73	53.88	15.93	34.71	0.00	0.00	0.00	57.93	1.41	147.92
E50-6-B3	3	0.192	11.0	7.89	41.09	3.74	19.48	0.00	0.00	0.00	88.32	0.05	148.94
E50-6-B4	4	0.459	11.0	8.90	19.39	4.08	8.89	0.00	0.00	0.00	86.92	0.09	115.29
E50-6-B5	5	0.726	11.0	14.89	20.51	8.31	11.45	0.00	4.57	6.29	71.66	0.57	110.48
SITE ID	Mg	Si	Fe	Al	Cu	Si_sub	Si_res	Al_sub	Al_con		RES:SUB	Mg:Si	
E50-6-B1	23.6	13.1	0.0	8.1	54.7	2.7	10.3	4.6	3.5		0.55	2.28	
E50-6-B2	36.4	23.5	0.0	0.0	39.2	2.0	21.5	0.0	0.0		1.41	1.69	
E50-6-B3	27.6	13.1	0.0	0.0	59.3	3.0	10.1	0.0	0.0		0.61	2.73	
E50-6-B4	16.8	7.7	0.0	0.0	75.4	3.8	3.9	0.0	0.0		0.26	4.27	
E50-6-B5	18.6	10.4	0.0	5.7	64.9	3.2	7.1	5.4	0.3		0.35	2.61	

SUBSTRATE	Mg	Si	Fe	Al	Cu	other	totals						
sub_1	0.00	3.42	0.00	7.49	89.09	0.00	100.00						
sub_2	0.00	4.44	0.00	8.33	87.23	0.00	100.00						
sub_3	0.00	5.37	0.00	6.27	88.36	0.00	100.00						
sub_avg	0.00	4.41	0.00	7.36	88.23	0.00	100.00						
SITE ID	loc#	SF	V	Mg	Mg_sca	Si	Si_sca	Fe	Al	Al_sca	Cu	other	total
E50-6-C1	1	0.726	10.5	9.81	13.51	3.25	4.48	0.86	9.50	13.09	76.58	0.00	108.51
E50-6-C2	2	0.459	10.5	52.34	114.03	22.23	48.43	2.10	0.00	0.00	23.33	0.00	187.89
E50-6-C3	3	0.192	10.5	9.75	50.78	2.34	12.19	1.25	0.00	0.00	86.65	0.00	150.87
E50-6-C4	4	0.459	10.5	14.56	31.72	3.46	7.54	1.54	0.00	0.00	80.45	0.00	121.25
E50-6-C5	5	0.726	10.5	17.26	23.77	6.07	8.36	0.72	6.41	8.83	69.54	0.00	111.22
SITE ID	Mg	Si	Fe	Al	Cu	Si_sub	Si_res	Al_sub	Al_con		RES:SUB	Mg:Si	
E50-6-C1	12.5	4.1	0.8	12.1	70.6	3.5	0.6	5.9	6.2		0.17	20.83	
E50-6-C2	60.7	25.8	1.1	0.0	12.4	0.6	25.2	0.0	0.0		6.67	2.41	
E50-6-C3	33.7	8.1	0.8	0.0	57.4	2.9	5.2	0.0	0.0		0.66	6.46	
E50-6-C4	26.2	6.2	1.3	0.0	66.4	3.3	2.9	0.0	0.0		0.44	9.02	
E50-6-C5	21.4	7.5	0.6	7.9	62.5	3.1	4.4	5.2	2.7		0.37	4.87	
SITE ID	loc#	SF	V	Mg	Mg_sca	Si	Si_sca	Fe	Al	Al_sca	Cu	other	total
E50-7-AE1	1	0.726	4.6	32.37	44.59	9.56	13.17	0.51	0.00	0.00	57.55	0.00	115.81
E50-7-AE2	2	0.459	4.6	20.70	45.10	4.58	9.98	1.10	0.00	0.00	73.62	0.00	129.80
E50-7-AE3	3	0.192	4.6	37.67	196.20	10.19	53.07	1.20	0.00	0.00	50.95	0.00	301.42
E50-7-AE4	4	0.459	4.6	52.66	114.73	19.13	41.68	2.11	0.00	0.00	26.09	0.00	184.61
E50-7-AE5	5	0.726	4.6	40.85	56.27	11.58	15.95	0.71	0.00	0.00	46.87	0.00	119.80
SITE ID	Mg	Si	Fe	Al	Cu	Si_sub	Si_res	Al_sub	Al_con		RES:SUB	Mg:Si	
E50-7-AE1	38.5	11.4	0.4	0.0	49.7	2.5	8.9	0.0	0.0		0.92	4.33	
E50-7-AE2	34.7	7.7	0.8	0.0	56.7	2.8	4.9	0.0	0.0		0.68	7.16	
E50-7-AE3	65.1	17.6	0.4	0.0	16.9	0.8	16.8	0.0	0.0		4.63	3.88	
E50-7-AE4	62.1	22.6	1.1	0.0	14.1	0.7	21.9	0.0	0.0		5.74	2.84	
E50-7-AE5	47.0	13.3	0.6	0.0	39.1	2.0	11.4	0.0	0.0		1.43	4.13	

SUBSTRATE	Mg	Si	Fe	Al	Cu	other	totals						
sub_1	0.00	3.42	0.00	7.49	89.09	0.00	100.00						
sub_2	0.00	4.44	0.00	8.33	87.23	0.00	100.00						
sub_3	0.00	5.37	0.00	6.27	88.36	0.00	100.00						
sub_avg	0.00	4.41	0.00	7.36	88.23	0.00	100.00						
SITE ID	loc#	SF	V	Mg	Mg_sca	Si	Si_sca	Fe	Al	Al_sca	Cu	other	total
E50-8-I1	1	0.726	8.5	45.98	63.33	14.82	20.41	0.95	0.00	0.00	38.25	0.00	122.95
E50-8-I2	2	0.459	8.5	20.81	45.34	4.77	10.39	1.78	0.00	0.00	72.00	0.00	129.51
E50-8-I3	3	0.192	8.5	20.79	108.28	5.19	27.03	1.51	0.00	0.00	72.52	0.00	209.34
E50-8-I4	4	0.459	8.5	45.64	99.43	16.70	36.38	1.54	6.68	14.55	29.44	0.00	181.35
E50-8-I5	5	0.726	8.5	21.10	29.06	12.10	16.67	1.06	8.32	11.46	42.12	0.00	100.37
SITE ID	Mg	Si	Fe	Al	Cu	Si_sub	Si_res	Al_sub	Al_con		RES:SUB	Mg:Si	
E50-8-I1	51.5	16.6	0.8	0.0	31.1	1.6	15.0	0.0	0.0		2.06	3.42	
E50-8-I2	35.0	8.0	1.4	0.0	55.6	2.8	5.2	0.0	0.0		0.71	6.67	
E50-8-I3	51.7	12.9	0.7	0.0	34.6	1.7	11.2	0.0	0.0		1.75	4.63	
E50-8-I4	54.8	20.1	0.8	8.0	16.2	0.8	19.3	1.4	6.7		4.07	2.85	
E50-8-I5	29.0	16.6	1.1	11.4	42.0	2.1	14.5	3.5	7.9		0.94	2.00	
SITE ID	loc#	SF	V	Mg	Mg_sca	Si	Si_sca	Fe	Al	Al_sca	Cu	other	total
E50-8-P1	1	0.726	7.5	41.72	57.47	14.42	19.86	1.08	5.32	7.33	49.09	0.00	134.83
E50-8-P2	2	0.459	7.5	20.19	43.99	4.67	10.17	1.29	0.00	0.00	72.49	0.00	127.94
E50-8-P3	3	0.192	7.5	30.04	156.46	7.36	38.28	1.28	0.00	0.00	71.01	0.00	267.03
E50-8-P4	4	0.459	7.5	52.63	114.66	19.65	42.81	1.65	0.00	0.00	42.75	0.00	201.87
E50-8-P5	5	0.726	7.5	33.41	46.02	10.43	14.37	1.03	7.23	9.96	40.10	0.00	111.47
SITE ID	Mg	Si	Fe	Al	Cu	Si_sub	Si_res	Al_sub	Al_con		RES:SUB	Mg:Si	
E50-8-P1	42.6	14.7	0.8	5.4	36.4	1.8	12.9	3.0	2.4		1.37	3.30	
E50-8-P2	34.4	8.0	1.0	0.0	56.7	2.8	5.1	0.0	0.0		0.68	6.71	
E50-8-P3	58.6	14.3	0.5	0.0	26.6	1.3	13.0	0.0	0.0		2.58	4.50	
E50-8-P4	56.8	21.2	0.8	0.0	21.2	1.1	20.1	0.0	0.0		3.50	2.82	
E50-8-P5	41.3	12.9	0.9	8.9	36.0	1.8	11.1	3.0	5.9		1.31	3.72	

SUBSTRATE	Mg	Si	Fe	Al	Cu	other	totals						
sub_1	0.00	3.42	0.00	7.49	89.09	0.00	100.00						
sub_2	0.00	4.44	0.00	8.33	87.23	0.00	100.00						
sub_3	0.00	5.37	0.00	6.27	88.36	0.00	100.00						
sub_avg	0.00	4.41	0.00	7.36	88.23	0.00	100.00						
SITE ID	loc#	SF	V	Mg	Mg_sca	Si	Si_sca	Fe	Al	Al_sca	Cu	other	total
E50-8-N1	1	0.726	7.9	33.86	46.64	10.22	14.08	0.70	6.14	8.46	49.09	0.00	118.96
E50-8-N2	2	0.459	7.9	19.72	29.89	3.27	7.12	3.98	6.53	14.23	72.49	0.00	127.71
E50-8-N3	3	0.192	7.9	17.20	89.58	4.14	21.56	2.36	5.29	27.55	71.01	0.00	212.07
E50-8-N4	4	0.459	7.9	35.12	76.51	11.20	24.40	1.03	9.90	21.57	42.75	0.00	166.26
E50-8-N5	5	0.726	7.9	36.54	50.33	11.53	15.88	0.79	11.04	15.21	40.10	0.00	122.31
SITE ID	Mg	Si	Fe	Al	Cu	Si_sub	Si_res	Al_sub	Al_con		RES:SUB	Mg:Si	
E50-8-N1	39.2	11.8	0.6	7.1	41.3	2.1	9.8	3.4	3.7		1.06	4.01	
E50-8-N2	23.4	5.6	3.1	11.1	56.8	2.8	2.7	4.7	6.4		0.45	8.54	
E50-8-N3	42.2	10.2	1.1	13.0	33.5	1.7	8.5	2.8	10.2		1.37	4.97	
E50-8-N4	46.0	14.7	0.6	13.0	25.7	1.3	13.4	2.1	10.8		2.06	3.44	
E50-8-N5	41.2	13.0	0.6	12.4	32.8	1.6	11.3	2.7	9.7		1.43	3.63	
SITE ID	loc#	SF	V	Mg	Mg_sca	Si	Si_sca	Fe	Al	Al_sca	Cu	other	total
E50-7-M1-1	1	0.726	8.0	33.85	45.94	10.21	14.06	1.09	0.00	0.00	55.36	0.00	116.45
E50-7-M1-2	2	0.459	8.0	27.61	60.15	7.57	16.49	2.22	0.00	0.00	62.61	0.00	141.47
E50-7-M1-3	3	0.192	8.0	14.07	73.28	3.53	18.39	2.35	3.01	15.68	77.03	0.00	186.72
E50-7-M1-4	4	0.459	8.0	23.62	51.46	6.67	14.53	0.53	4.87	10.61	64.30	0.00	141.43
E50-7-M1-5	5	0.726	8.0	28.02	38.60	8.47	11.67	0.55	0.00	0.00	62.96	0.00	113.77
SITE ID	Mg	Si	Fe	Al	Cu	Si_sub	Si_res	Al_sub	Al_con		RES:SUB	Mg:Si	
E50-7-M1-1	39.4	12.1	0.9	0.0	47.5	2.4	9.7	0.0	0.0		1.00	4.07	
E50-7-M1-2	42.5	11.7	1.6	0.0	44.3	2.2	9.4	0.0	0.0		1.15	4.50	
E50-7-M1-3	39.2	9.8	1.3	8.4	41.3	2.1	7.8	3.4	5.0		1.03	5.04	
E50-7-M1-4	36.4	10.3	0.4	7.5	45.5	2.3	8.0	3.8	3.7		0.87	4.55	
E50-7-M1-5	33.9	10.3	0.5	0.0	55.3	2.8	7.5	0.0	0.0		0.72	4.53	

SUBSTRATE	Mg	Si	Fe	Al	Cu	other	totals						
sub_1	0.00	3.42	0.00	7.49	89.09	0.00	100.00						
sub_2	0.00	4.44	0.00	8.33	87.23	0.00	100.00						
sub_3	0.00	5.37	0.00	6.27	88.36	0.00	100.00						
sub_avg	0.00	4.41	0.00	7.36	88.23	0.00	100.00						
SITE ID	loc#	SF	V	Mg	Mg_sca	Si	Si_sca	Fe	Al	Al_sca	Cu	other	total
E50-7-M2-1	1	0.726	8.0	34.07	46.93	10.55	14.53	0.82	0.00	0.00	54.56	0.00	116.84
E50-7-M2-2	2	0.459	8.0	9.51	20.72	2.02	4.40	0.00	0.00	0.00	88.47	0.00	113.59
E50-7-M2-3	3	0.192	8.0	32.32	168.33	10.34	53.85	1.04	0.00	0.00	56.30	0.00	279.53
E50-7-M2-4	4	0.459	8.0	13.71	29.87	3.36	7.32	0.00	0.00	0.00	82.92	0.00	120.11
E50-7-M2-5	5	0.726	8.0	12.78	17.60	3.86	5.32	0.00	0.00	0.00	80.59	0.70	104.21
SITE ID	Mg	Si	Fe	Al	Cu	Si_sub	Si_res	Al_sub	Al_con		RES:SUB	Mg:Si	
E50-7-M2-1	40.2	12.4	0.7	0.0	46.7	2.3	10.1	0.0	0.0		1.04	3.98	
E50-7-M2-2	18.2	3.9	0.0	0.0	77.9	3.9	0.0	0.0	0.0		0.22	####	
E50-7-M2-3	60.2	19.3	0.4	0.0	20.1	1.0	18.3	0.0	0.0		3.73	3.30	
E50-7-M2-4	24.9	6.1	0.0	0.0	69.0	3.5	2.6	0.0	0.0		0.38	9.41	
E50-7-M2-5	16.9	5.1	0.0	0.0	77.3	3.9	1.2	0.0	0.0		0.22	13.66	
SITE ID	loc#	SF	V	Mg	Mg_sca	Si	Si_sca	Fe	Al	Al_sca	Cu	other	total
E50-7-M3-1	1	0.726	8.0	16.88	23.25	4.87	6.71	0.00	0.00	0.00	78.25	0.00	108.21
E50-7-M3-2	2	0.459	8.0	15.54	33.86	3.73	8.13	1.91	0.00	0.00	78.82	0.00	122.71
E50-7-M3-3	3	0.192	8.0	15.54	80.94	3.59	18.70	0.00	0.00	0.00	80.87	0.00	180.51
E50-7-M3-4	4	0.459	8.0	27.22	59.30	8.98	19.56	0.90	4.98	10.85	57.82	0.00	148.44
E50-7-M3-5	5	0.726	8.0	10.35	14.26	2.14	2.95	0.00	0.00	0.00	87.51	0.70	105.41
SITE ID	Mg	Si	Fe	Al	Cu	Si_sub	Si_res	Al_sub	Al_con		RES:SUB	Mg:Si	
E50-7-M3-1	21.5	6.2	0.0	0.0	72.3	3.6	2.6	0.0	0.0		0.32	8.31	
E50-7-M3-2	27.6	6.6	1.6	0.0	64.2	3.2	3.4	0.0	0.0		0.48	8.09	
E50-7-M3-3	44.8	10.4	0.0	0.0	44.8	2.2	8.1	0.0	0.0		1.13	5.52	
E50-7-M3-4	40.0	13.2	0.6	7.3	39.0	1.9	11.2	3.3	4.1		1.17	3.56	
E50-7-M3-5	13.5	2.8	0.0	0.0	83.0	4.1	-1.4	0.0	0.0		0.14	-9.99	

SUBSTRATE	Mg	Si	Fe	Al	Cu	other	totals						
sub_1	0.00	3.42	0.00	7.49	89.09	0.00	100.00						
sub_2	0.00	4.44	0.00	8.33	87.23	0.00	100.00						
sub_3	0.00	5.37	0.00	6.27	88.36	0.00	100.00						
sub_avg	0.00	4.41	0.00	7.36	88.23	0.00	100.00						
SITE ID	loc#	SF	V	Mg	Mg_sca	Si	Si_sca	Fe	Al	Al_sca	Cu	other	total
E50-7-AB1	1	0.726	3.7	45.94	63.28	17.59	24.23	1.52	0.00	0.00	34.95	0.00	123.98
E50-7-AB2	2	0.459	3.7	48.80	106.32	22.39	48.78	3.96	0.00	0.00	24.85	0.00	183.91
E50-7-AB3	3	0.192	3.7	46.94	244.48	20.36	106.04	5.20	0.00	0.00	27.50	0.00	383.22
E50-7-AB4	4	0.459	3.7	45.47	99.06	16.43	35.80	2.02	0.00	0.00	36.07	0.00	172.95
E50-7-AB5	5	0.726	3.7	51.67	71.17	24.68	33.99	2.23	0.00	0.00	21.41	0.70	129.51
SITE ID	Mg	Si	Fe	Al	Cu	Si_sub	Si_res	Al_sub	Al_con		RES:SUB	Mg:Si	
E50-7-AB1	51.0	19.5	1.2	0.0	28.2	1.4	18.1	0.0	0.0		2.38	2.81	
E50-7-AB2	57.8	26.5	2.2	0.0	13.5	0.7	25.8	0.0	0.0		6.05	2.24	
E50-7-AB3	63.8	27.7	1.4	0.0	7.2	0.4	27.3	0.0	0.0		12.27	2.34	
E50-7-AB4	57.3	20.7	1.2	0.0	20.9	1.0	19.7	0.0	0.0		3.57	2.91	
E50-7-AB5	55.0	26.2	1.7	0.0	16.5	0.8	25.4	0.0	0.0		4.73	2.16	